

AN ABSTRACT OF THE THESIS OF

Andrew M. Vincent III for the degree of Master of Science
in Nuclear Engineering presented on Dec. 9, 1981

Title: Fuel-Cladding Mechanical Interaction In
Simulated Sphere Pac Fuel

Abstract Approved: Redacted for Privacy

K. L. Peddicord

A study has been made to investigate the fuel-cladding mechanical interaction (FCMI) in sphere pac fuels. An FCMI simulation has been constructed using the JVG Apparatus. This model has been used to investigate the mechanical interaction between a sphere pac bed and a cladding wall in terms of the cladding surface stresses and strains. Two measurement techniques were used to obtain these quantities; photoelastic coatings and strain gages.

A variety of sphere pac beds were used. A primary consideration was the presence or absence of an infiltrating size fraction. For the cases in which this is absent, the load transmission to the cladding shows a high degree of non-uniformity. When an infiltrating fraction is present, the aforementioned phenomena is greatly mitigated. The surface stress distribution arising from a sphere contact consistently appeared as an "hourglass" shape

with shear stress maximum values occurring along the vertical axis of the apparatus.

Several analytic approaches were taken to model the tube hoop strains. In a very simplistic method, the fuel region was approximated as an incompressible fluid. The most successful approximation was to treat the sphere packed as a cohesionless, granular medium and proceed as in a rock mechanics solution.

Fuel-Cladding Mechanical Interaction in
Simulated Sphere Pac Fuel

by

Andrew M. Vincent III

A THESIS

submitted to

Oregon State University

in partial fulfillment of
the requirements for the
degree of

Master of Science

Completed December 9, 1981

Commencement June, 1983

APPROVED:

Redacted for Privacy

Professor of Nuclear Engineering in Charge of Major

Redacted for Privacy

Head of Department of Nuclear Engineering

Redacted for Privacy

Dean of Graduate School

Date thesis is presented December 9, 1981

Typed by A. M. Vincent for A. M. Vincent

ACKNOWLEDGEMENT

I would like to thank my funding agency, EIR, the Swiss Federal Institute for Reactor Research, for their generous support of this work.

Particular thanks go to my major professor, Dr. K.L. Peddicord, whose enthusiasm and encouragement were an inspiration, and whose sense of humor will never go unappreciated.

Special thanks to Dr. Tim Kennedy and Tom George who guided me through the maze of stress analysis.

Thanks also go to my predecessors in this effort, C.W. Bennett, J. Van-Gulik, and B.A. Waggener, without whose efforts this project may have gone in unknown directions.

Last, but certainly not least, thanks to my very supportive family and friends who never had any doubts and never questioned my need for 540,000 steel balls.

TABLE OF CONTENTS

1.	Introduction.....	1
1.1	Motivation.....	1
1.2	Background.....	1
2.	Test Facility Description.....	3
2.1	The Apparatus.....	3
2.2	Experimental Test Matrix.....	9
3.	Measurement Techniques.....	11
3.1	Strain-Gage Methods.....	11
3.2	Photoelastic Coating Methods.....	16
4.	Data Acquisition and Reduction.....	28
4.1	Expansion Bladder Performance.....	28
4.2	Cladding Modulus of Elasticity.....	31
4.3	Practicability Studies.....	37
4.4	Photoelastic Data Reduction.....	45
4.5	Bulk Data Presentation.....	52
5.	Analysis and Discussion of Results.....	67
5.1	Comparative Analysis.....	67
5.2	Results.....	78
5.3	Conclusions.....	92
	Bibliography.....	98
	Appendix.....	100

LIST OF FIGURES

Figure		Page
2.1	JVG Apparatus.....	5
2.2	JVG Apparatus.....	6
4.1	Pump Pressure vs. Diameter Change.....	30
4.2	Cladding Modulus of Elasticity.....	33
4.3	Cladding Modulus of Elasticity.....	34
4.4	Cladding Poissons Ratio.....	36
4.5	Test 1.....	38
4.6	Test 2.....	40
4.7	Coating 1 Calibration.....	44
4.8	Coating 2 Calibration.....	48
4.9	Coating 3 Calibration.....	49
4.10	Coating 4 Calibration.....	50
4.11	Test 3a.....	53
4.12	Test 3b.....	54
4.13	Test 3c.....	55
4.14	Gage Response.....	56
4.15	Test 4.....	57
4.16	Test 5.....	58
4.17	Test 6.....	59
4.18	Test 7.....	60
5.1	Coarse Fraction Simulation.....	81
5.2	Coarse Fraction Simulation.....	82

List of Figures (continued)

Figure		Page
5.3	Coarse plus Fine Simulation.....	84
5.4	Coarse plus Fine Simulation.....	85
5.5	Coarse plus Medium Simulation.....	86
5.6	Coarse plus Medium Simulation.....	87
5.7	Coarse, Medium, and Fine Simulation.....	90
5.8	Coarse, Medium, and Fine Simulation.....	91
5.9	Flat Wall Approximation.....	94
5.10	Shear Distribution on a Cylinder Wall.....	94
5.11	Shear Maxima Separation on a Cylinder Wall..	95

LIST OF TABLES

Table	Page
2.1 Sphere Sizes and Types with Comparative Values.....	7
2.2 Physical Characteristics of Sphere Pac Fuels: (U,Pu)C, UO ₂ , and Simulated.....	8
2.3 Test Matrix.....	9
3.1 Dominant Isochromatic Fringe Colors and Approximate Relative Retardation for Full-Field Interpretation.....	23
4.1 Photoelastic Coating Thicknesses and Areas.....	42
4.2 Parameters for Photoelastic Correction Factor.....	47
4.3 Calibration Constants for Photoelastic Coating.....	51
4.4 Corrected Strains for Photoelastic Measurements (coating #3: P = 200 psi, 1" + 1/10", Batch 2).....	62
4.5 Corrected Strains for Photoelastic Measurements (coating #4: P = 200 psi, 1" + 1/10", Batch 2).....	62
4.6 Corrected Strains for Photoelastic Measurements (coating #3: P = 170 psi, 1" + 5/16", Batch 5).....	63
4.7 Corrected Strains for Photoelastic Measurements (coating #3: P = 210 psi).....	63
4.8 Corrected Strains for Photoelastic Measurements (approximate maximum values: 1" + 5/16").....	64
4.9 Corrected Strains for Photoelastic Measurements (approximate maximum values: 1" only)...	64
4.10 Corrected Strains for Photoelastic Measurements (coating #3: LWR, Batch 8).....	65
4.11 Corrected Strains for Photoelastic Measurements (coating #4: LWR, Batch 8).....	66

List of Tables (continued)

Table	Page
5.1 Predicted Strain Values Assuming Compressible Fluid and Accounting for Hose Pressure Drop.....	72
5.2 Predicted Strain Value Using Rock Mechanics Solution (steel balls only).....	75
5.3 Predicted Strain Value Using Rock Mechanics Solution (steel plus alumina).....	75

FUEL-CLADDING MECHANICAL INTERACTION IN SIMULATED SPHERE PAC FUEL

Chapter I: Introduction

1.1 Motivation

Fuel-cladding mechanical interaction (FCMI) in nuclear fuel rods is an important consideration in assessing the behavior of pellet fuel rods. Operating experience has attributed cladding failure to a large extent to this interaction in boiling water reactors (BWR's), CANDU reactors, and in some cases, pressurized water reactors (PWR's) (ref. 1). Hence fuel-cladding interaction appears to be a generic fuel failure mechanism for BWR and PWR zircaloy cladding UO_2 fuel rods. This phenomena then must necessarily be examined for sphere pac nuclear fuels being developed for fast reactor and thermal reactor use. This is the objective of this study.

1.2 Background

Two basic types of sphere pac fuels are being investigated for power reactor applications. For fast reactors, a two size fraction combination of (U,Pu)C spheres (800 μm and 60 μm diameters) is proposed. For light water reactors, three-size fraction UO_2 is used

consisting of spheres 1200 μm , 400 μm , and 25-40 μm in diameter.

For these fuel types, the large scale mechanical interaction between a packed bed and a tube wall has been simulated with a laboratory scale model, the JVG apparatus (ref. 2). The apparatus has been designed and constructed to investigate the local cladding wall stress and strain resulting from an expanding packed sphere bed. The model basically has preserved the cladding-diameter-to-sphere-diameter ratios used in the development of the sphere pac fuel concept. Where the sphere-to-sphere ratios are concerned, the preservation of diameter ratios also exists quite closely, most importantly observing the relation of infiltrating versus non-infiltrating size fractions.

Chapter 2: Test Facility Description

2.1 The Apparatus

The FCMI simulation test facility, originally designed and fabricated by J. Van-Gulik and B.A. Waggener (ref. 3), consists of a central expanding bladder which transmits a load radially through an annular sphere packed bed to the cladding wall. The annulus is of sufficient radius and height so as to avoid edge or wall effects (ref. 4). Axial constraints exist in such a fashion so as to transmit the bladder load entirely radially as opposed to allowing axial displacement as well as radial expansion.

The central bladder is a 30 in. section of reinforced rubber hose having an outside diameter of 4.5 in. and a wall thickness $3/16$ in. This type and size of hose is typically capable of withstanding internal pressures of 400-600 psi in a freestanding mode (ref. 5). For applications such as the FCMI tests, this maximum pressure will be considerably higher due to the constraints imposed upon the hose by the packed particle bed.

The cladding was originally fabricated from $7/32$ in. galvanized sheet metal with a diameter of 10 in. and a height of 18 in. Due to reasons to be discussed in chapter 4, this was replaced with an acrylic material with the same overall dimensions but with a thickness of $3/16$ in.

The central bladder is held in a vertical position by a stationary frame. The dimensional details are described in figures 2.1 and 2.2. The frame was fabricated from 3/16 in. steel square tubing with a base made of 3/16 in. boiler plate. The acrylic cladding was maintained with the same centerline axis as the bladder through the static loading of the packed particle bed. Again, axial displacement was constrained by fixed end plates.

The radial force transmitted to the sphere pac bed was applied hydraulically through the expandable bladder using an Ener-pac hand pump having an operating range of 0-300 psi (ref. 6). However, the experimental pressure range only required a maximum of approximately 220 psi to achieve the desired strain levels. The pump-bladder connection was through use of a 3/16 in. rubber hose and quick connect-disconnect fittings.

To approximate the fuel types in consideration, namely the two-size-fraction carbide fast reactor fuel and the three-size-fraction oxide light water reactor fuel, materials were chosen to maintain the proper cladding diameter to sphere ratios. The materials were chosen based on several factors: (1) size and material properties, and (2) cost and availability. The material sizes and types are listed in Table 2.1 with comparative values for the actual cases.

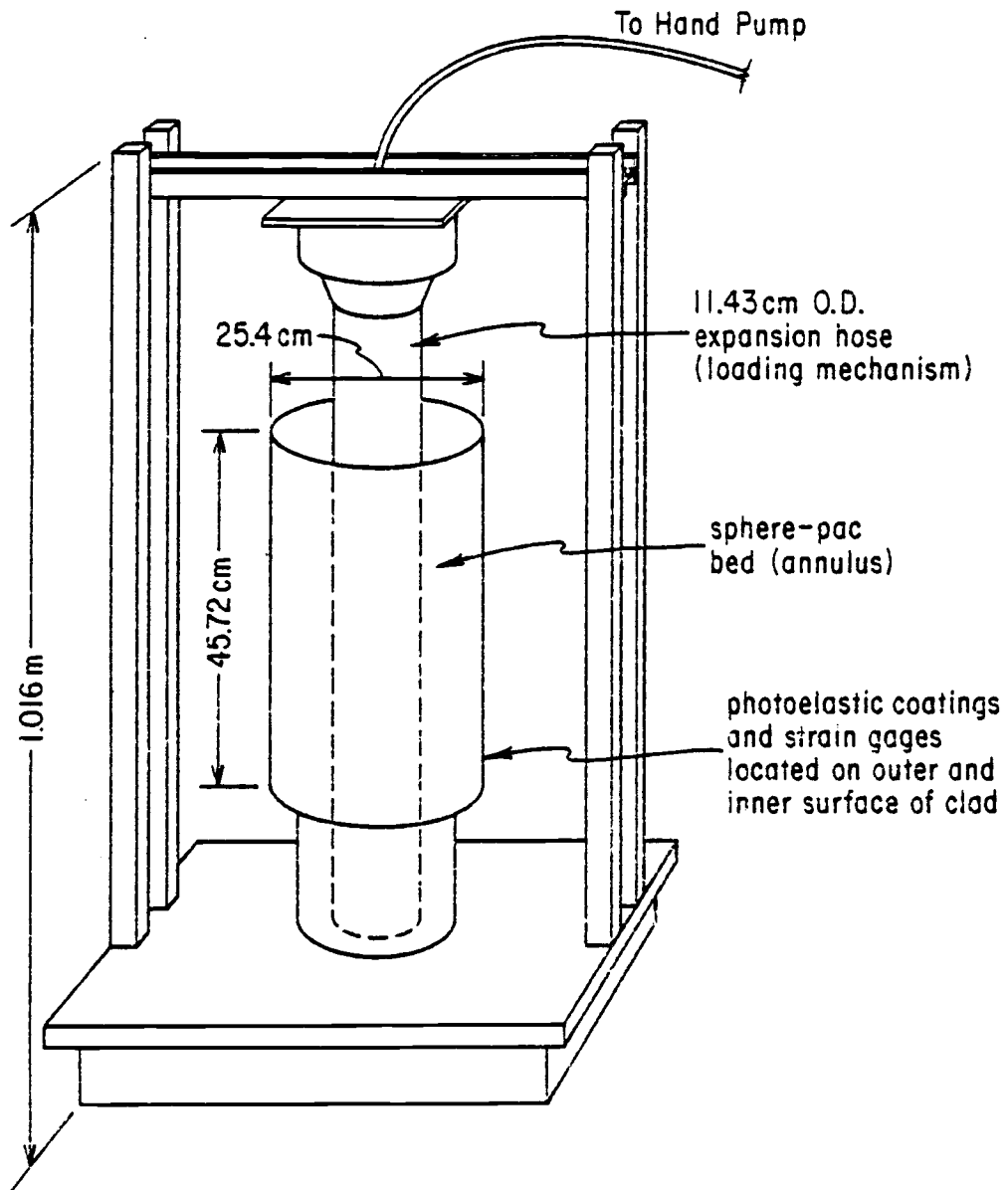


Figure 2.1. JVG Apparatus.

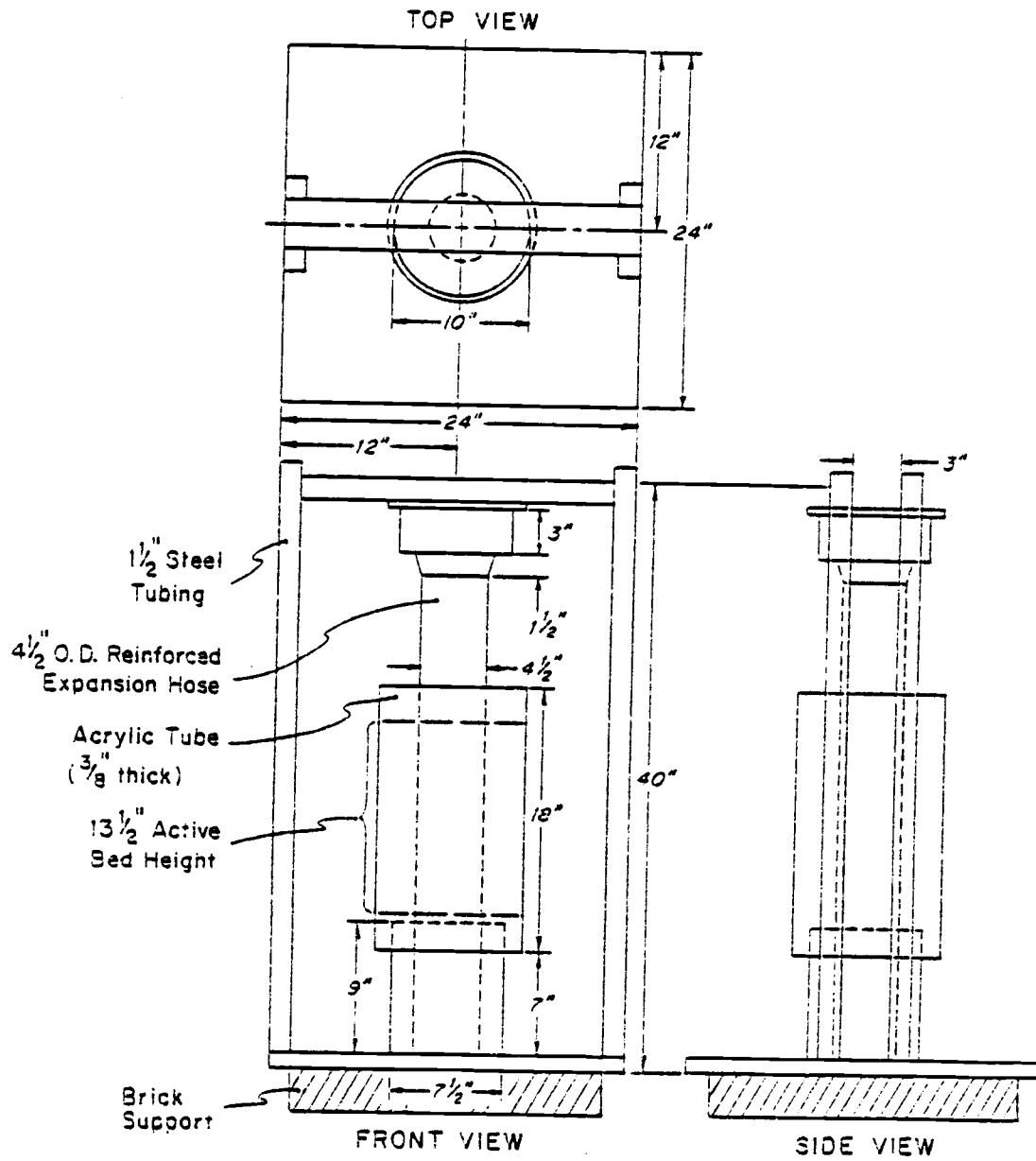


Figure 2.2. JVG Apparatus.

Table 2.1

<u>Size (μm)</u>	<u>Material</u>	<u>Simulation</u>	<u>Material</u>
LMFBR:			
800	(U,Pu)C	2.54 cm	Carbon steel
60	" "	0.254 cm	" "
LWR:			
1200	UO	2.54 cm	" "
400	"		" "
25-40	"	500 μm	alumina

In selecting the various fuel simulation constituents, the characteristics desired were: (1) the cladding diameter to large fraction sphere diameter, and (2) the large fraction to secondary constituents relations. By this it is meant that approximate ratios have been preserved, but more importantly, the ability of a smaller size sphere to infiltrate a larger sphere matrix has been preserved. This is the case in the LMFBR combination (1 to 1/10 sphere diameter ratio) and in the LWR combination (1 to 500 μm and 1 to 5/16 diameter ratios), approximating the actual infiltrating beds.

It is recognized that the materials and their respective sizes do not coincide directly with those of the actual fuel. However, the macroscopic FCMI properties of

this system provide qualitative indications of the response of the actual two- and three-size fraction fuels. Useful quantitative indications are provided of the relative response in going from one bed type to another.

Further comparative information is provided in Table 2.2.

Table 2.2

Physical Characteristics of Sphere Pac Fuels:
(U,Pu)C, UO₂, and Simulated

<u>Fuel Type</u>	<u>Packing Factor (%)</u>	<u>Smear Density (%)</u>
(U,Pu)C	coarse...62.5	80.78
	fine.....56.7	
(U,Pu)C	coarse...60.0	78.4
	simulation	
	fine.....54.0	
UO ₂	coarse...50.94	
	medium...39	86.6
	fine.....35	
UO ₂	coarse...51	
simulation	medium...25	-
	fine.....30	

2.2 Experimental Test Matrix

The specific test cases investigated involved basically the two-size-fraction fast reactor fuel simulation, the three-size-fraction light water reactor fuel simulation, and variations within these two types (refer to Table 2.3). The first case consists solely of the coarse (1 in. diameter) sphere pac bed. Due to the relatively large separation between spheres at the cladding wall, this bed provides clearly a basis for all other cases investigated and therefore a relatively distinct strain pattern at the cladding outer surface where measurement is made.

Table 2.3

Test Matrix

Cases

1. 1" sphere bed
2. 1" + 1/10" bed (LMFBR)
3. 1" + 5/16" + 1/40" bed (LWR)
4. 1" + 5/16" bed

Tests

1. Photoelastic coatings
2. Strain gages
3. Oblique incidence for fringe order resolution into principal components
4. Photography for data recording

The measurement techniques used to analyze these test cases were primarily strain gages and photoelastic coating, or photostress methods. Detail is provided on these topics in chapter 3 and in the appendix.

Chapter 3: Measurement Techniques

In the fuel-cladding mechanical interaction simulation, a load is placed upon the acrylic cladding by an expanding bed of spheres. It is desired to measure the resulting stresses and strains which will provide the information for an assessment of the FCMI models in a sphere pac bed system. The result is essentially a biaxial stress state in the cladding, and the measurement of the stress must be addressed with this in mind.

Current applied stress analysis techniques offer a number of alternatives for application to a given situation. Of these methods, two approaches were selected based on the information they provide and the ease with which they may be used. These are namely electrical resistance strain gages and photostress or photoelastic coatings. This chapter reviews the application of these techniques as they apply to FCMI simulation.

3.1 Strain Gage Methods

Electrical resistance strain gages have been developed to provide accurate measurements of normal strain. Strain-measuring transducers measure the average normal strain along some gage length rather than strain at a point. If the gage length is kept small, errors associated with

such measurements can be kept within acceptable limits. The installation and operating characteristics of a strain gage are affected by the following parameters, which are selectable in varying degrees (ref. 7):

- strain-sensitive alloy
- backing (carrier) material
- gage length
- gage pattern (number, arrangement, and orientation of grids)
- self-temperature compensation number
- grid resistance

The gage selection process consists of determining the particular available combination of parameters which is most compatible with the environmental and other operating conditions, and at the same time best satisfies the installation and operation constraints. These constraints are generally expressed in the form of requirements such as:

- accuracy
- stability
- maximum elongation
- test duration
- cyclic endurance
- simplicity and ease of installation

In making a selection for the FCMI model, the test conditions were stated as static, room temperature, maximum strain or elongation unknown, and acrylic cladding. Given these conditions, the gage selected had a designation:

CEA-41-125AC-350

The CEA designates a flexible-polyimide backing material with a constantan foil grid strain sensing alloy in self-temperature compensated form. The 41 indicates a coefficient of thermal expansion of 41 PPM/°F which closely approximates the coefficient for the acrylic cladding. The tests are run at room temperature. However, a temperature change can be introduced simply from gage heating due to resistance. This is an effect localized at the gage area and can be minimized by increasing the gage resistance, in this case to 350 ohms (ref. 7). Concerning grid size, a length of 0.125 in. was chosen as the smallest suitable size due to a degraded performance in gages of less than this length particularly in terms of the maximum allowable elongation and stability under static strain.

Due to the geometry of the model and the mode of loading, the directions of the principal axes were approximately known so that single grid gages could be used. These were mounted in approximate coincidence with these axes to yield the maximum strain at that location.

Prior to test performance the gages were tested to measure two important properties of the installations; insulation resistance, and the deviation of the gage resistance from its nominal resistance. Both these measurements can be influenced by improper installation procedures. To accomplish this test, a Vishay Instruments Model 1300 Gage Installation Tester was used (ref. 8). There are two ranges possible in the deviation mode; $\Delta 1\%$ and $\Delta 5\%$. In the 1% range the accuracy is $0.04\% \Delta R$, and in the 5% range, $0.2\% \Delta R$. In the insulation resistance mode, it is a 5 Mohm to 20000 Mohm graduated scale with 1 scale division of accuracy.

Given a proper installation, the gage is placed in a Wheatstone bridge circuit. For this purpose, a Vishay/Ellis 10 Portable Strain Indicator was used (ref. 9). This instrument is primarily a resistance bridge for measurement of static strain. Internal batteries power the measuring bridge and the null amplifier. The null amplifier, a direct-coupled transistor amplifier, drives a taut-band microammeter to display the polarity and relative magnitude of the bridge unbalance.

Two-arm external circuits, or a single compensated gage, can be measured with the Ellis 10. An internal 120 ohm resistor is provided for use with strain gages of the nominal value. For gages of other than 120 ohm, the circuit may be modified by the addition of a bridge completion

resistor of the desired ohmage, in this instance, 350 ohm to comply with the gages used on the test part.

Measurements are made by observing differences between the dial settings required to null the bridge for various loads. For single gages with gage factors in the range 1.95 to 2.05, the dial is direct reading. Gage factor is defined as

$$(\Delta R/R)/(\Delta L/L) \quad (3-1)$$

where R = resistance in ohms

L = gage length

The gage factor of the gages used in these experiments was 2.05.

For measurement of a set of gages, a Vishay Portable Switch and Balance Unit, Model 1012, was used (ref. 10). This unit is designed primarily to provide a method to sequentially read the outputs of up to six channels of strain gage information on a single indicator such as the V/E 10. Each channel can be initially balanced to read zero (or other cardinal reading) to simplify data interpretation and reduction. It offers full isolation for each individual circuit, thus preventing the catastrophic failure of one channel from affecting results from other channels.

A separate ten-turn, high-resolution potentiometer, with added friction to maintain settings, is provided for setting the initial reading for each of the six inputs.

Where it is known that a load will produce either tension or compression, the initial reading is set at zero. Where the load will produce an unknown result, the initial reading is set at 5000 μ in/in to allow for a tensile or compressive measurement.

3.2 Photoelastic Coating Methods

The method of birefringent coatings, also called the method of photoelastic coatings, extends the classical procedures of model photoelasticity to the measurement of surface strains in opaque two- and three-dimensional models made of any structural material. The coating is a thin layer of birefringent material, usually a polymer, that is bonded integrally to the flat or curved surfaces of the prototype being analyzed for stress. When the prototype is loaded, the surface strains are transmitted to the coating, reproducing the prototype strain field in the coating. In these experiments, the prototype strain field is affected by the presence of the coating, so that coating thickness correction factors are required to account for this effect. To provide light reflection at the interface, the coating is bonded in place with a reflective cement. When viewed through a white-light reflection polariscope, the strained coating exhibits black isoclinic and colored isochromatic fringes. Isoclinic fringes provide directions of principal strains. Isochromatic fringes, when viewed in normal

incidence light, provide the difference of principal strains (maximum shear strains); when viewed in oblique-incidence light, they provide additional data that permit the determination of the magnitude and sign of individual principal strains. Full-field isochromatic and isoclinic patterns are directly visible and can be photographed for subsequent analysis by using simple reflection polariscopes.

When a photoelastically coated test object is subjected to loads, the resulting stresses induced strains to exist generally throughout the part and over its surface. The surface stresses and strains are commonly the largest, and of the greatest importance. This is the case in the FCMI model both at the inner and the outer surfaces of the cladding. Due to the intimate bond between the coating and the cladding, the strains in the cladding are faithfully transmitted to the coating. The strains in the coating produce proportional optical effects which appear as isochromatic fringes when viewed with a reflection polariscope.

Applying the load or loads incrementally, fringes will appear first at the points of highest stress. As the load is increased, the fringes move toward areas of lower stress and more fringes appear at the high stress points. The fringes can be assigned a fixed ordinal number as they

appear. These fringes are ordered and continuous, i.e., they never cross or merge with one another.

The fringe orders observed in photoelastic coatings are proportional to the difference between the principal strains in the coating (and in the surface of the test part). The relationship is expressed as

$$\epsilon_x - \epsilon_y = fN_n \quad (3-2)$$

where ϵ_x, ϵ_y = principal strains in the coating and test part,

f = fringe value of the coating expressed in (in/in/fringe)

N_n = fringe order; observed birefringence in fringe units.

In terms of shear strain,

$$\gamma_{xy} = fN \quad (3-3)$$

γ = maximum shear strain (in the plane of the test part at any point)

Transformation of equations (3-2) and (3-3) using the biaxial Hookes' law expresses the results in terms of stress as

$$\sigma_x = \frac{E}{1 - \nu^2} (\epsilon_x + \nu\epsilon_y) \quad (3-4)$$

$$\sigma_y = \frac{E}{1 - \nu^2} (\epsilon_y + \nu\epsilon_x) \quad (3-5)$$

and
$$\sigma_x - \sigma_y = \frac{E}{1 - \nu^2} (\epsilon_x - \epsilon_y) \quad (3-6)$$

Substituting (3-2) into (3-6) yields

$$\sigma_x - \sigma_y = \frac{E}{1 + \nu} fN \quad (3-7)$$

where σ_x, σ_y = principal stresses in the test part surface,

E = elastic modulus of the test part, and

ν = Poisson's ratio of the test part.

Noting that the maximum shear stress, τ_m , in the plane of the surface at any point is given by $(\sigma_x - \sigma_y)/2$,

$$\tau_m = 0.5 \left(\frac{E}{1 + \nu} \right) fN \quad (3-8)$$

These quantities can be obtained by a single fringe order measurement in normal incidence. To determine the individual magnitudes and signs of principal strains or stresses generally requires, for biaxial stress states, a second measurement of fringe order in oblique incidence. This technique is somewhat similar to the 3-gage rosette, where one measures in different directions to deduce maximum strains and their direction.

When light propagates in the plane of one of the principal stresses, σ_y , at an angle θ to the normal, the fringe order observed becomes

$$N_\theta f = \frac{1 - \nu \cos^2 \theta}{(1 + \nu) \cos \theta} \epsilon_x - \frac{\cos^2 \theta - \nu}{(1 - \nu) \cos^2 \theta} \epsilon_y \quad (3-9)$$

One already has from equation (3-2)

$$N_n f = \epsilon_x - \epsilon_y$$

Combining the normal and oblique incidence measurements (eq.'s (3-2) and (3-9)) gives

$$\epsilon_x = f \left[N_\theta \frac{(1-\nu) \cos \theta}{(1+\nu) \sin^2 \theta} - N_n \frac{\cos^2 \theta - \nu}{(1+\nu) \sin^2 \theta} \right] \quad (3-10)$$

$$= f \left[N_\theta \frac{(1-2) \cos \theta}{(1+2) \sin^2 \theta} - N_n \frac{1-\nu \cos \theta}{(1+2) \sin^2 \theta} \right] \quad (3-11)$$

The values N_θ and N_n are obtained by use of a reflection polariscope, in this case an 030-series model manufactured by Photoelastics, Inc. (ref. 11). The foundation component of the 030-series polariscope is the optical head, which consists of two polarizer/quarter-wave plate assemblies attached to a common frame. These assemblies are coupled for synchronous rotation (ref. 11).

The optical assembly is equipped to receive any of several light sources. For the present application, a minimum-weight light, with a prefocused internal-reflector projection lamp (white light) in a self-ventilating housing. The assembly includes a linear polarizer and quarter-wave retardation plate, and serves as the source of (circularly) polarized light for illuminating the photoelastic coating. The second optical assembly also contains a linear polarizer and quarter-wave retardation plate, and functions as the

analyzer through which the coating is observed to measure the strain. All polariscope controls and measuring scales are incorporated in the analyzer.

The identification of fringe orders requires knowledge of the optical response of a birefringent material to stress. The optics are discussed in Appendix A, a general discussion being presented here.

Under white light, the photoelastic fringe pattern appears as a series of successive and contiguous, different colored bands (isochromatics) in which each band represents a different degree of birefringence corresponding to the underlying strain in the test part. Thus, the color of each band uniquely identifies the birefringence, or fringe order (and strain level), everywhere along that band. With an understanding of the unvarying sequence in which the colors appear, the photoelastic pattern can be read to visualize the stress distribution over the surface of the coated test part.

The color pattern is caused by the attenuation and extinction of one or more colors from the white-light spectrum, and the observed colored fringes represent the complementary colors produced by the transmitted portion of the spectrum. Table 3.1 illustrates the sequence of colored fringes produced in a field with linearly increasing stress magnitude for full-field interpretation.

In addition to the identification of the integral fringes accomplished by correct identification of the isochromatics is the determination of fractional fringe order. Compensation techniques are necessary for precise fringe-order determination where the highest fringe order is less than two and a resolution of 5 percent is required in the analysis. Compensation methods are point-by-point methods and require additional operations by the investigator.

Table 3.1

Dominant Isochromatic Fringe Colors and
Approximate Relative Retardation for
Full-Field Interpretation

<u>Color</u>	<u>Retardation</u>	<u>Fringe Order</u>
Black	0	0
Yellow	345	.6
Red	520	.9
Purple*	575	1.0
Blue-Green	700	1.22
Green-Yellow	800	1.39
Rose-Red	1050	1.82
Red/Green*	1150	2.00
Green	1350	2.35
Green-Yellow	1440	2.50
Red	1520	2.65
Red/Green*	1730	3.00
Green	1800	3.10

* The tint-of-passage corresponds to a full wavelength of relative retardation for a wavelength of 575 nm. This is a sharp dividing zone between red and blue in the first-order fringe, red and green in the second-order fringe, and pink and green in the third-, fourth-, and fifth- order fringes. Beyond five fringes, white light is not adequate.

There are two basic approaches to compensation. In the first, compensation is achieved by converting the elliptically polarized light emerging from the photoelastic medium into linearly polarized light and then extinguishing this light by rotation of the analyzer. The angle of

rotation of the analyzer from its dark field position is proportional to the fractional fringe order measured. This method is known as Tardy compensation (ref. 12). The accuracy of this method is about 0.05 fringe.

With the second approach to compensation, another birefringent element is inserted in series with the photoelastic model. The birefringence in this element can be adjusted to provide a retardation equal in magnitude and opposite in sign to that occurring in the photoelastic model. When the adjustment of the compensating element is complete, the net birefringence in the light path is zero and the point under consideration is observed as black in the field of the polariscope. This method is known as null balance compensation and has a resolution of 0.01 fringe (ref. 12).

For the purposes of this study, high resolution or accuracy is not required. Financial considerations, viz. the cost of a null balance compensator coupled with the accuracy requirements, suggests that Tardy compensation is quite adequate for the FCMI studies. This is the method used for fractional fringe order determination in these tests.

As in the case of electrical resistance strain gages, photoelastic coating materials are available in a variety of designations to conform to a given situation. The principal

considerations in the selection of a photoelastic plastic for a specified set of test conditions are:

1. method of application
2. sensitivity
3. contour severity
4. reinforcing effect
5. maximum elongation
6. test temperature

Of these considerations, perhaps the single most important factor is the birefringent sensitivity of the plastic material, since it is involved in the basic equation governing photoelastic coating analysis;

$$\epsilon_1 - \epsilon_2 = \gamma_m = Nf \quad (3-2)$$

$$\text{or} \quad n f = N \frac{\lambda}{2t_c K} \quad (3-12)$$

where λ = wavelength of light used in polariscope, taken as $22.7E-6$ in. for white light (ref. 12)

t_c = coating thickness, in.

K = strain-optic coefficient of the plastic material.

Assuming the number of fringes to be observed, and estimating the expected strain level, the corresponding coating sensitivity, or fringe value, may be calculated as follows;

$$f = \frac{\epsilon_1 - \epsilon_2}{N} = \frac{\gamma_m}{N} \quad (3-13)$$

$$= \frac{\text{Expected strain level}}{\text{max. number of fringes expected}}$$

Once the fringe value has been established from the expected strain level and number of fringes, the type and thickness of the plastic which will satisfy the sensitivity requirement can be determined from the relationship

$$f = \frac{\lambda}{2t_c K} \quad (3-14)$$

This has been plotted parametrically for convenience in (ref. 13).

From these basic considerations, the calculations of which may be found in Chapter 4, the following plastic selection was made:

Plastic designation: liquid PL-1

-- this is a high modulus material, room temperature curing plastic for casting contourable sheets. It exhibits high photo-elastic sensitivity and ample working time.

K (min): 0.01

Max. elongation (%): 3-5

E (1000 psi): 420

-- thickness limitations: for casting contourable sheets up to 0.125 in.

Adhesive designation: PC-1

-- provides excellent bond strength with absence of creep. Relatively fast curing time.

Cure time (hrs): 12

Cure temperature: room

Elongation (%): 3-5

E (1000 psi): 450

In both the selection of the liquid plastic and the adhesive, it is important to match closely the modulus of the test material. This simplifies computations and increases accuracy. The modulus of elasticity of the acrylic cladding is discussed in Chapter 4.

Chapter 4: Data Acquisition and Reduction

The acquisition of data for the FCMI tests was approached from several angles, with the end result governed primarily by the test matrix outlined in Chapter 2 (table 2.2). Before these experiments were performed, a number of tests were carried out to provide vital information regarding material properties, apparatus performance characteristics, and viability studies for the test apparatus and the measurement techniques.

With this data, the experiments were performed which provided the results found at the end of this chapter and chapter 5. The form in which the results appear in this chapter is primarily graphical and calculational. The calculations involve the correction of data for various effects as discussed in chapter 3 and also the interpretation of data to give various constants (properties) required for further analysis.

These topics will be approached in the order of their appearance in this introduction which is also the sequence in which they were performed.

4.1 Expansion Bladder Performance

The consideration of importance in the use of the central expansion hose is the axial uniformity of expansion with increasing hydraulic pressure (see chap. 2). The bladder itself is a reinforced rubber hose, operated in its

elastic range as described in chapter 2. These types of hoses are tested to pressures of approximately 500 psi in an unconstrained mode (ref. 14). The range of test pressures approached 220 psi but in a constrained mode owing to the presence of the sphere pac bed. This constraint also maintained the axis of expansion during the primary tests.

To examine the performance characteristics of this expansion system, measurements of the diameter of the hose were taken at several locations within the bed region with increasing pressure. The pressure range was that of the FCMI test range, namely 0-200 psi.

The results indicate very uniform expansion over the length of the bed region, as shown in figure 4.1. The curve is non-linear, but this feature is of no consequence, again due to the constraint induced on the expansion system by the sphere pac bed. What is of importance is the uniform axial response of the system to pressure.

The modeling of the fuel-cladding mechanical interaction in a sphere pac bed is predicated on the internal force exerted on the cladding wall which is transmitted through the bed matrix. In an actual case fuel pin, this force is due to the thermal expansion of the fuel. Greater expansion is seen in the central regions of the fuel bed, due to the much higher temperatures produced there. It is this phenomena, or rather the forces produced by this phenomena that are being modeled in this work.

PUMP PRESSURE vs DIAMETER CHANGE*

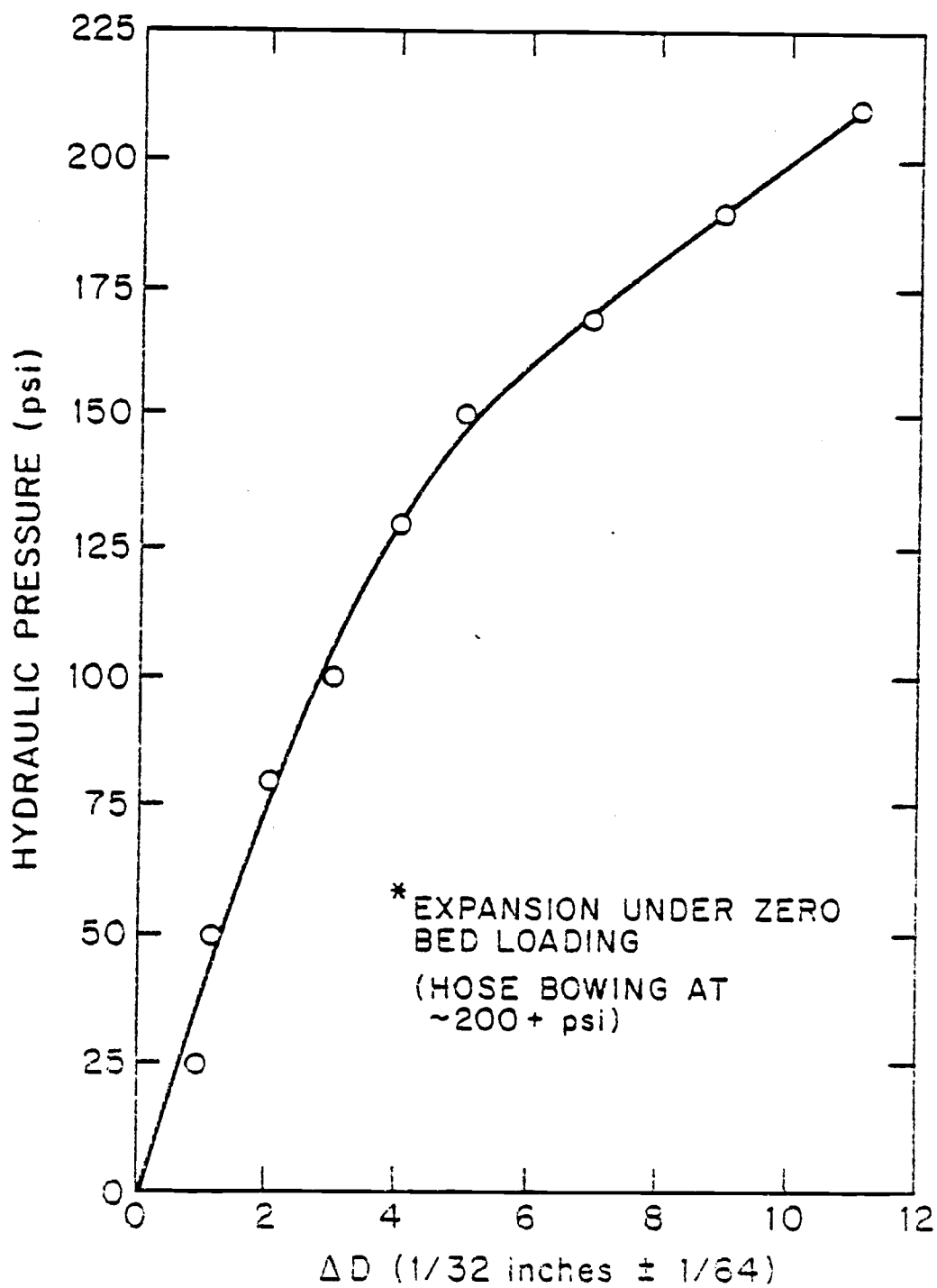


Figure 4.1

4.2 Cladding Modulus of Elasticity

The modulus of elasticity and Poisson's ratio arise often in stress analysis calculations. Certainly the current work is no exception. In these experiments the values are necessary both in the photoelastic coating work and in analytic work to be presented in chapter 5.

The method of determination of these values was a simple tensile test. The tests were performed on a Tate Emery Testing Machine which simply applies a specified load (tensile or compressive) to a specimen.

Several specimens were prepared from an acrylic tube of the same set of tubes as were used in the experiments. Their dimensions were 10 in. X 1/2 in. X 3/16 in.

Two measurement techniques were employed to measure the change in length, ΔL . Of lesser importance, due to its low accuracy and relatively short strain range, was a dial gauge. This method resulted in a sporadic set of values. The second method, strain gages, gave a very precise set of results for both the modulus of elasticity and Poisson's ratio calculations. From these results, a value was determined.

The load range was from 0-300 lb. Incremental loading was performed at intervals of 4 or 10 lb. Two tests were considered as invalid due to inaccuracies in measurement of L (tests ME1 and ME2). A yield strength was determined from

test ME1, however, that value being of only incidental value except to say that it is sufficiently high (> 300 lb) that it will not be of concern in the experiments.

The strain gages were of the type described in chapter 3. For the modulus determination, a simple axial alignment of the gage on the tensile specimen was used. For the Poisson's ratio determination, one axially aligned and one horizontally aligned strain gage was used.

Based on these measurements, the following calculations were made:

-- from figure 4.2,

cross-sectional area, $A = 0.0938 \text{ in}^2$

$\Delta\epsilon = 2300 \text{ in/in}$

$\Delta P = 104 \text{ lb}$

$$\text{therefore, } E = \frac{\Delta P}{A_c \Delta \epsilon} \quad (4.1)$$

$$= 4.82 \times 10^5 \text{ psi}$$

-- from figure 4.3,

cross-sectional area, $A = 0.0938 \text{ in}^2$

$\Delta\epsilon = 2100 \mu\text{in/in}$

$\Delta P = 90 \text{ lb}$

$$\text{therefore, } E = \frac{\Delta P}{A_c \Delta \epsilon}$$

$$= 4.57 \times 10^5 \text{ psi}$$

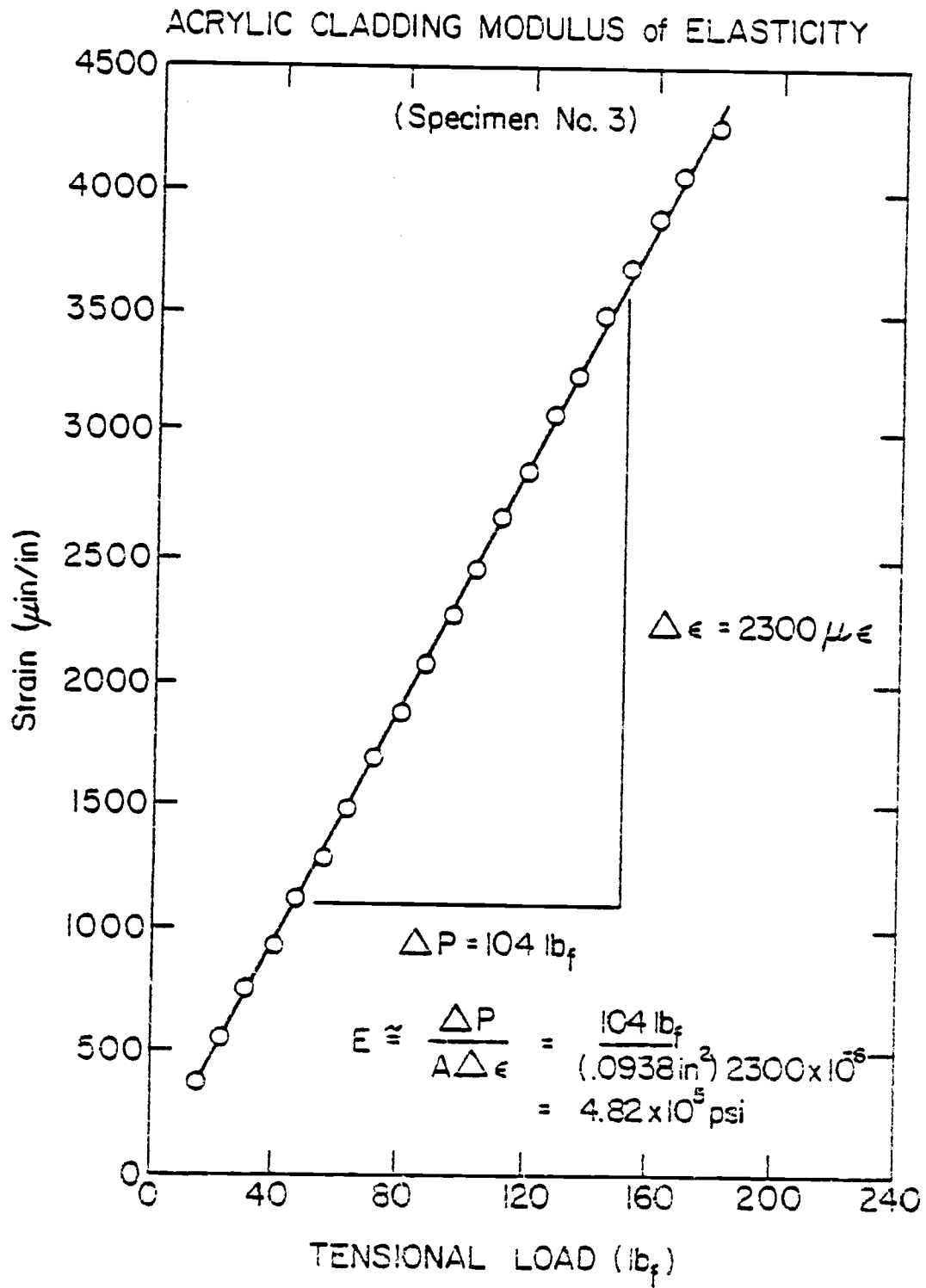


Figure 4.2

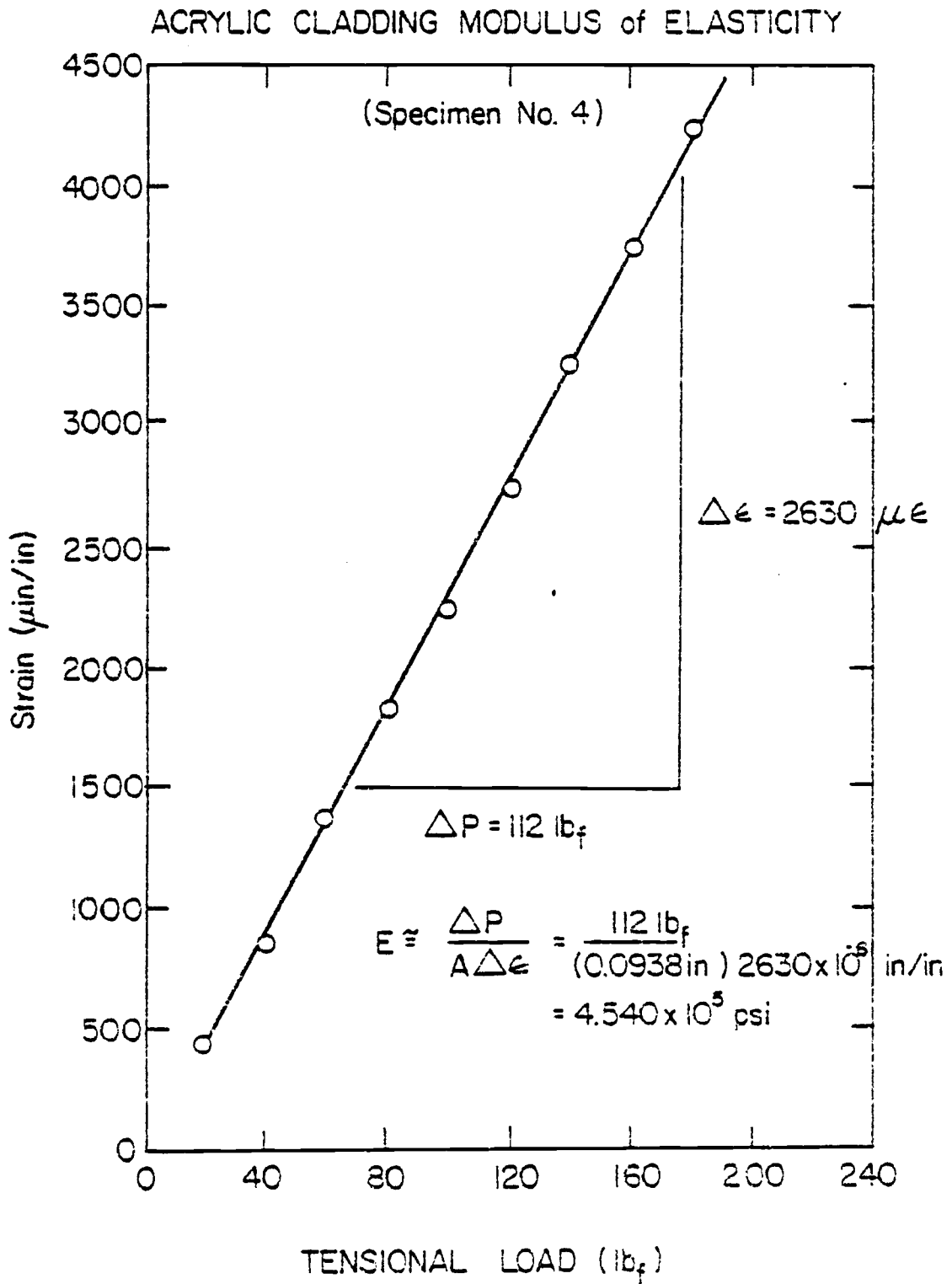


Figure 4.3

-- from figure 4.4,

$$\text{for } \Delta\epsilon_v = 2830 \text{ } \mu\text{in/in}$$

$$\Delta\epsilon_h = -1000 \text{ } \mu\text{in/in}$$

Poisson's ratio, (4.2)

$$\begin{aligned} \nu &= - \frac{\Delta\epsilon_h}{\Delta\epsilon_v} \\ &= 0.353 \end{aligned}$$

The manufacturer/supplier of the acrylic tubes also provided data representative of cast acrylic materials (ref. 15). These values are representative of those obtained under standard ASTM conditions and represent average values. For comparison to the experimental results in this report, the following modulus of elasticity in tension is given;

$$E = 3.5 - 5.0 (X 10^5) \text{ psi}$$

and tensile strength = 8000 - 11000 psi.

From the above calculations, the modulus was determined to be

$$E = 4.57 - 4.82 (X 10^5) \text{ psi}$$

and tensile strength = 3200 psi.

The modulus value fell into the predicted range. The tensile strength was considerably below its predicted value, however. This is thought to be due to the method of

ACRYLIC CLADDING POISSONS RATIO

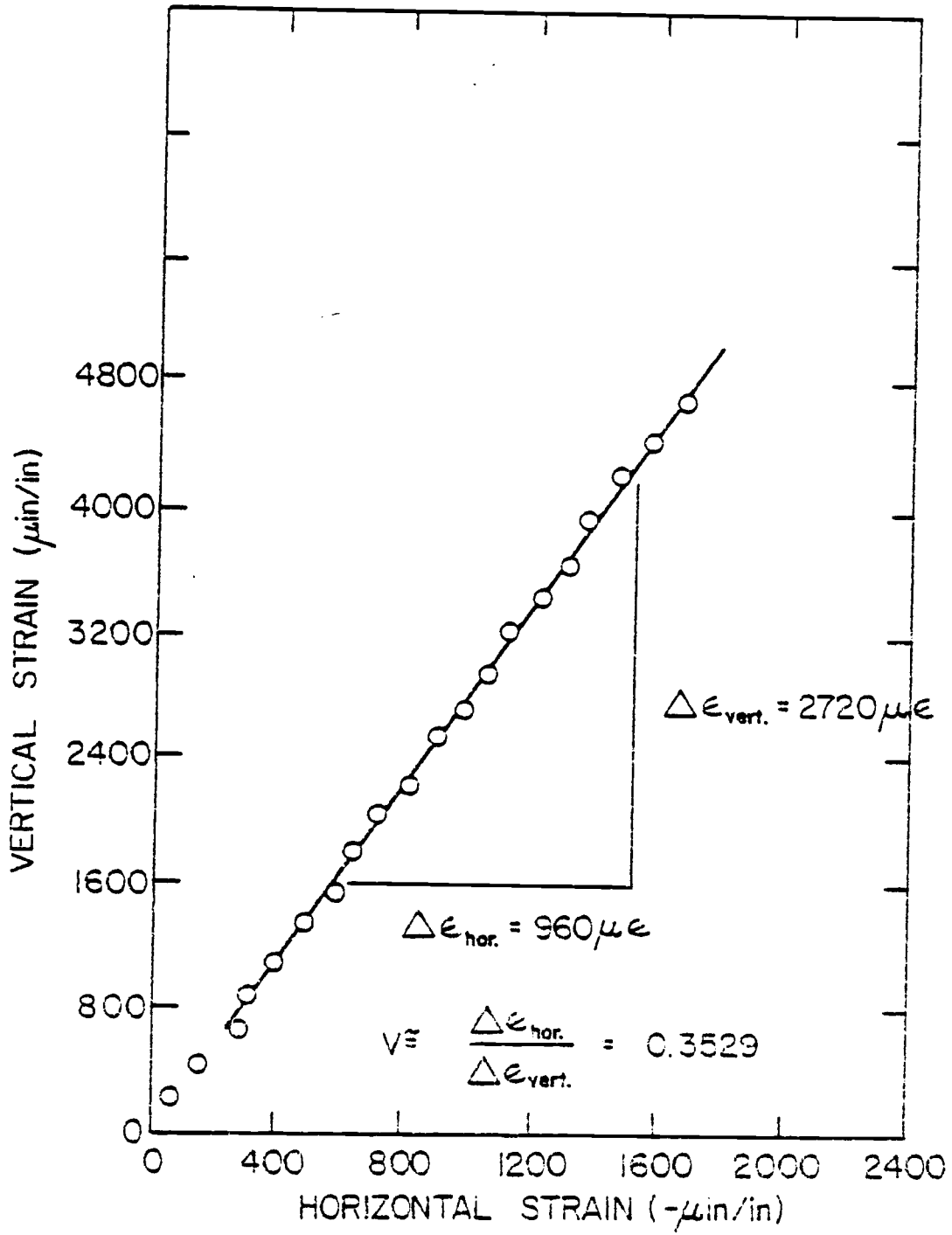


Figure 4.4

securing the specimen to the test apparatus, which may have hindered the results in this case.

4.3 Practicability Studies

These studies were simply intended to provide information regarding the viability of the measurement techniques as applied to the FCMI model. This includes the application of strain gages and their response to load changes, and photoelastic coating molding, contouring, bonding, and its subsequent performance in response to representative strain levels.

The strain gage testing was initiated with a series of 120 Ω resistance gages (designated Test 1). The bed was a matrix of 1 in. spheres in the apparatus annulus as described in chapter 2. This bed was then subjected to a load ascension in varying increments, the load ranging from 0-150 psi. The results were poor, i.e. sporadic response from gages 1, 4, 5, and 6, and no response from gage 3. Gage 2 seemingly performed adequately (see figure 4.5). Overall, the gage type compatibility and the installations were deemed inadequate.

Test 2 employed three 350 Ω resistance gages of the designation and description given in chapter 3. As in Test 1, a one inch sphere matrix was used with an incremental loading scheme in steps of 10 psi ranging from 0-140 psi. The gage locations were selected to provide representative strain values in the regions of interest for the particular

STRAIN (@ LOAD POINT) vs PUMP PRESSURE
(Initial loading: 1" spheres only,
gauge @ load point, 120 Ω)

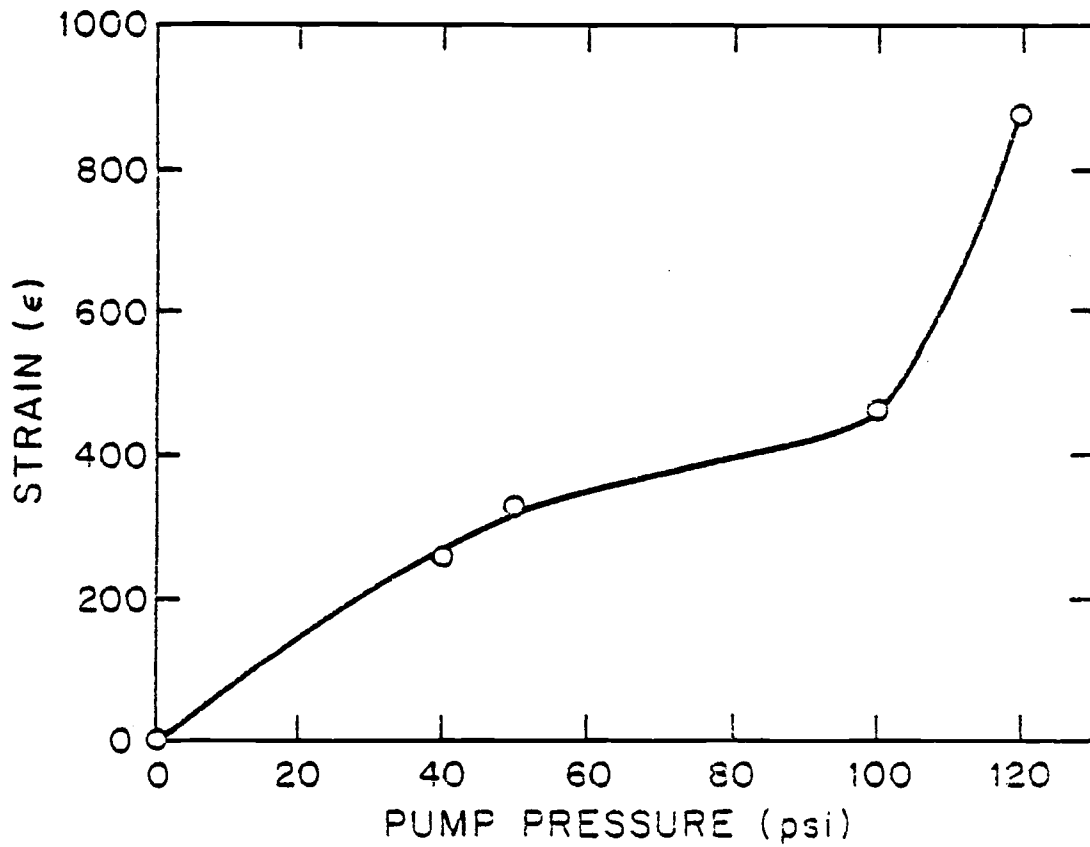


Figure 4.5

bed type. The results are presented graphically in figure 4.6.

Prior to test 2, and all subsequent gage operations, each installation was checked with the Model 1300 gage installation tester described in chapter 3. This provided verification of the ohmage and insulation properties of each gage.

The test 2 results demonstrated laudable response characteristics and thus testing proceeded with these gage types and installations.

Also considered part of the practicability studies was photoelastic coating #1. This involved the molding, contouring, and bonding of one 80-gram kit of the liquid plastic PL-1. The choice of plastic type and coating thickness was determined by first establishing a fringe value. From chapter 3 eq. (12);

$$f = \frac{\epsilon_1 - \epsilon_2}{N} = \frac{\gamma_m}{N} \quad (4.3)$$

Based upon the initial strain gage response,

$$\text{expected strain level} = 4000 \mu\text{in/in}$$

The maximum number of fringes expected is based upon the Photoelastic Division Technical Data Bulletin T-401-A Table 1 (ref. 13) which, for the given situation suggests the value of

$$N = 1-4 \text{ fringes}$$

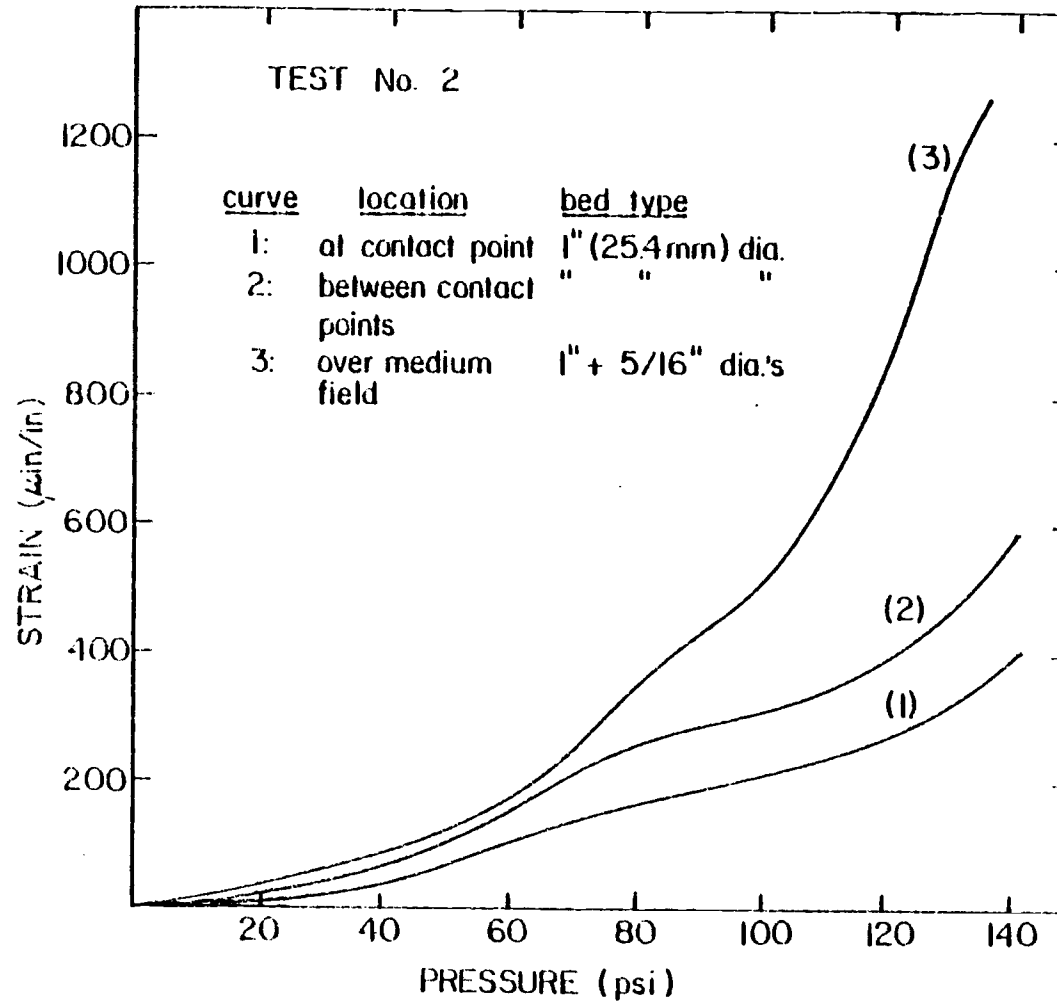


Figure 4.6

Using $\gamma_m = 4000 \mu \text{ in/in}$ and $N = 4$,

$$f = 4000 \times 10^{-6} = 1000 \mu \text{ in/in/fringe} \quad (4.4)$$

Having established the fringe order, or coating sensitivity, the type and thickness of the plastic which will satisfy the sensitivity requirement can be determined from

$$f = \frac{\lambda}{2t_{ck}} \quad (4.5)$$

This is plotted parametrically in (ref. 13), or, using the following values, coatings can be used of the types shown in table 4.1

$$\lambda(\text{white light}) = 22.7 \times 10^{-6} \text{ in}$$

$$K(\text{strain - optic coefficient}) = 0.1$$

and $f = 1000 \mu \text{ in/in/fringe}$

From Photoelastics Bulletin IB-221 (ref. 16) the sheet area may be calculated given an 80-gram kit of resin and hardener as

$$A = W/(18.5 \times t) \quad (4.6)$$

where $W = \text{total amount used (grams)}$

$A = \text{area of sheet (in}^2\text{)}$

$t = \text{desired thickness (in)}$

By varying the number of fringes desired, coating thicknesses and areas were determined:

<u>Fringes desired N</u>	<u>Coating thickness t (inches)</u>	<u>Area (side length in inches)</u>
2	0.1135	6 X 6.35
2.5	0.0908	6.8 X 7
3	0.0757	7.14 X 8
3.36	0.0676	8 x 8
3.5	0.0649	8 X 8.33

For the sake of convenience, the 8" x 8" sheet area was used after experimentation with the other various combinations.

Each coating requires a calibration for determination of the relevant properties of the installation. This is due to the fact that the values in table 4.1 are only predictive numbers to give general direction to the strain measurement to follow. In practice these values are slightly different.

The values to be ascertained in a calibration are: 1) the coating thickness, t_c ; 2) the strain-optic coefficient, K , which defines a fundamental property of the photoelastic material itself and is independent of the plastic thickness and the length of the light path; and, 3) the fringe value, f , specifying the strain-optic sensitivity of a particular photoelastic coating. The value f takes into account the

thickness of the coating, the fact that the light traverses the coating twice in reflection photoelasticity, and the nature of the light source.

The calibration basically consists of a cantilever beam upon which a specimen of the photoelastic coating is bonded. By then deflecting the beam a predetermined amount, a known state of strain is imposed upon the coating. Measurement of the resultant birefringence in the coating provides the information for relating fringe order to principal strain difference.

For the practicability studies of the photoelastic coating technique, the first coating was molded, contoured, and bonded with the following specifications;

thickness, $t = 0.1366$ in

area = 6×6.35 in²

The resulting curve (figure 4.7) gives

$$\frac{\Delta N}{\Delta D} = 4.52 \text{ fringes/in}$$

From the calibration chart for photoelastic coatings given the above specifications (ref. 11) the following constants were arrived at:

$$K = 0.082$$

$$f = 1100 \text{ } \mu\text{E/fringe}$$

Typical photoelastic plastics used in stress analysis of structural materials exhibit values of K from 0.08 to about 0.15, with the larger coefficients corresponding to

PHOTOELASTIC COATING No. 1: Calibration

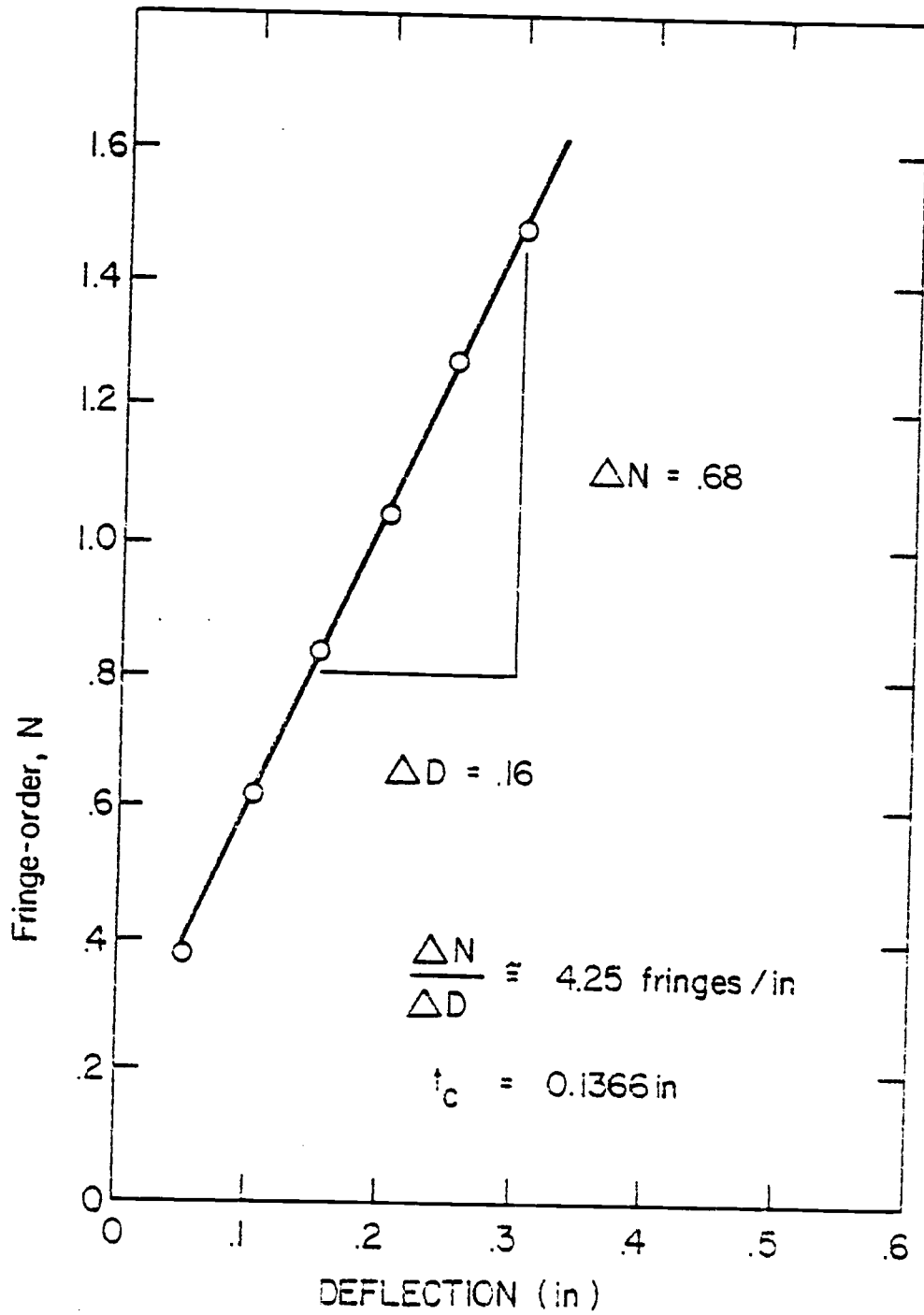


Figure 4.7

the optically sensitive materials. The fringe value, f , for most practical cases, will fall in the range from 500 to 3000 $\mu\text{in/in-fringe}$, with the low fringe values representing the more sensitive coatings.

From the values of K and f as determined experimentally for coating #1, and the load simulation tests involving the coating, the practicability of this stress analysis in the FCMI application was established.

4.4 Photoelastic Data Reduction

The use of the photoelastic coating technique requires several steps for the data reduction phase. For a given coating, a thickness value is recorded, and the coating calibrated as in section 4.3. With an increasing load on the model, a strain field appears at which time several points are selected for normal and oblique incidence fringe-order determination. The load is increased incrementally, and at each increment a slide was taken of the entire strain field and the fringe-order were measurements recorded. This continues until the desired maximum load is recorded.

The fringe-order measurements must be corrected for sources of error in the coating method. The principal sources are:

1. parasitic (initial) birefringence
2. reinforcement effects in plane stress systems

3. reinforcement and strain-extrapolation effects for plates in bending
4. temperature effects.

In the FCMI testing, item (3) results in significant error. This effect comes into the play when thin beams, plates, or shells are subjected to bending. This causes the effects of the photoelastic coating to be generally much greater than for the plane-stress case, and a correction is almost always required. The influence of the coating on a member-in-bending is quite complex, and the correction factor must account for three different effects as follows:

1. the neutral axis of the coated member is shifted toward the coated side.
2. the coating increases the stiffness of the member and decreases the deformation for a particular applied bending moment.
3. there is a strain (and fringe-order) gradient through the thickness of the coating.

All three effects operate simultaneously but are influenced differently by the elastic modulus and thickness ratios, E^* and t^* . A single correction factor is presented (ref. 11) as:

$$C_B = \frac{1 + E^*(4t^* + 6t^{*2} + 4t^{*3}) + E^{*2}t^{*4}}{1 + t^*} \quad (4.7)$$

where C_B = factor by which the observed fringe-order in bending must be multiplied to obtain the corrected fringe order

$$E^* = E_C/E_S$$

= ratio of the elastic modulus of the photoelastic coating to that of the specimen.

$$t^* = t_c / t_s$$

= ratio of the coating thickness to the specimen thickness.

Table 4.2, and the following constants provide the necessary information for these corrections:

specimen elastic modulus, E , = 0.47×10^6 psi

specimen thickness = 0.1875 in

coating elastic modulus, E , = 0.42×10^6 psi

Table 4.2

<u>coating</u>	<u>thickness</u>	<u>t</u>	<u>C</u>
1	0.1366	0.7285	6.1421
2	0.0803	0.4283	2.6761
3	0.0665	0.3547	2.2991
4	0.0681	0.3632	2.3406

Also necessary in the data reduction of the photoelastic information is the calibration constants for the given coating. Section 4.3 provides the background information for the calibration techniques. Once these values are obtained, and the corrections have been made to the fringe order values, the principal strains may be determined. Figures 4.8, 4.9, and 4.10 show the calibration curves for coatings 2, 3, and 4, respectively. Table 4.3 summarizes the values determined from these curves.

PHOTOELASTIC COATING No. 2: Calibration

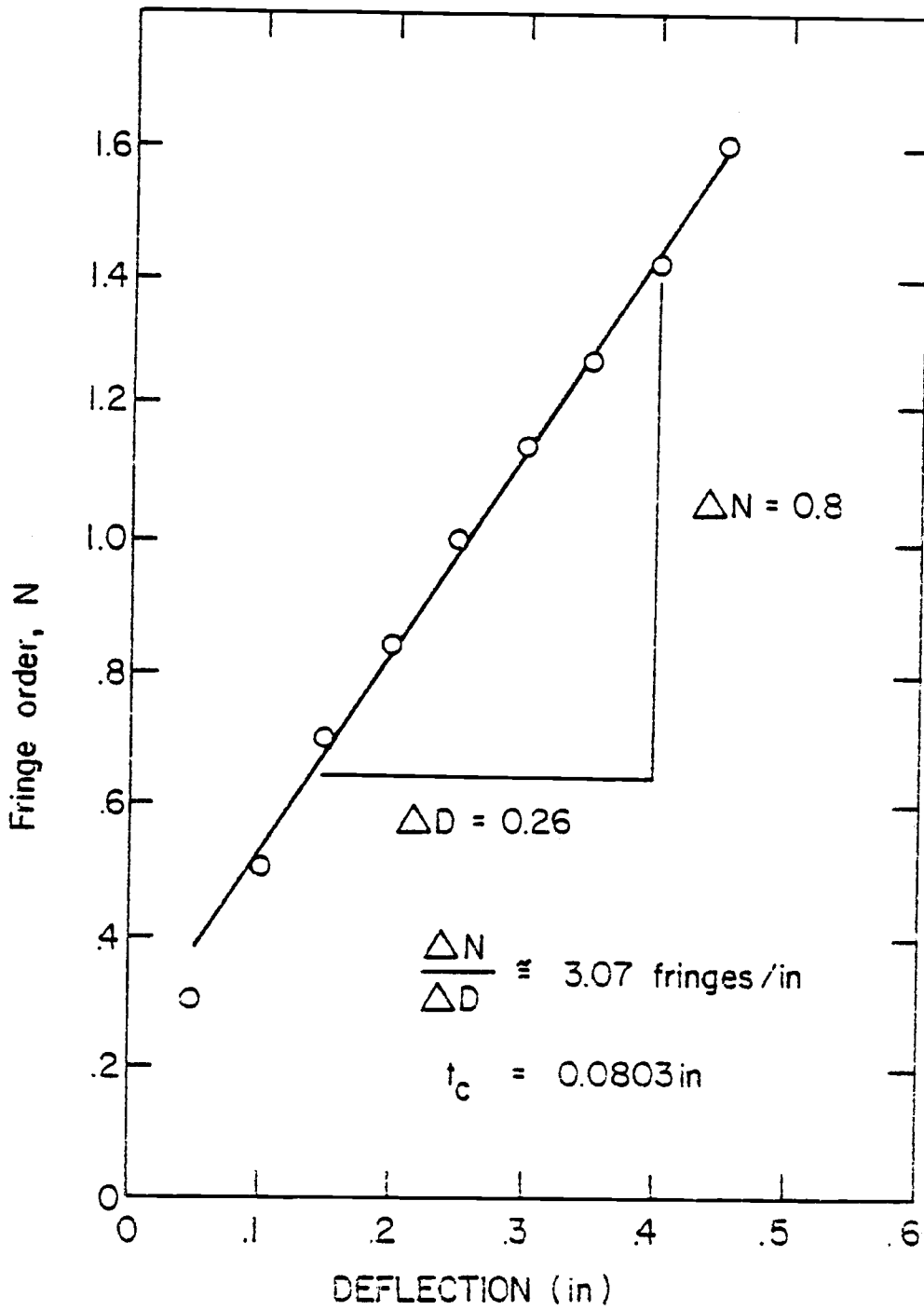


Figure 4,8

PHOTOELASTIC COATING No. 3: Calibration

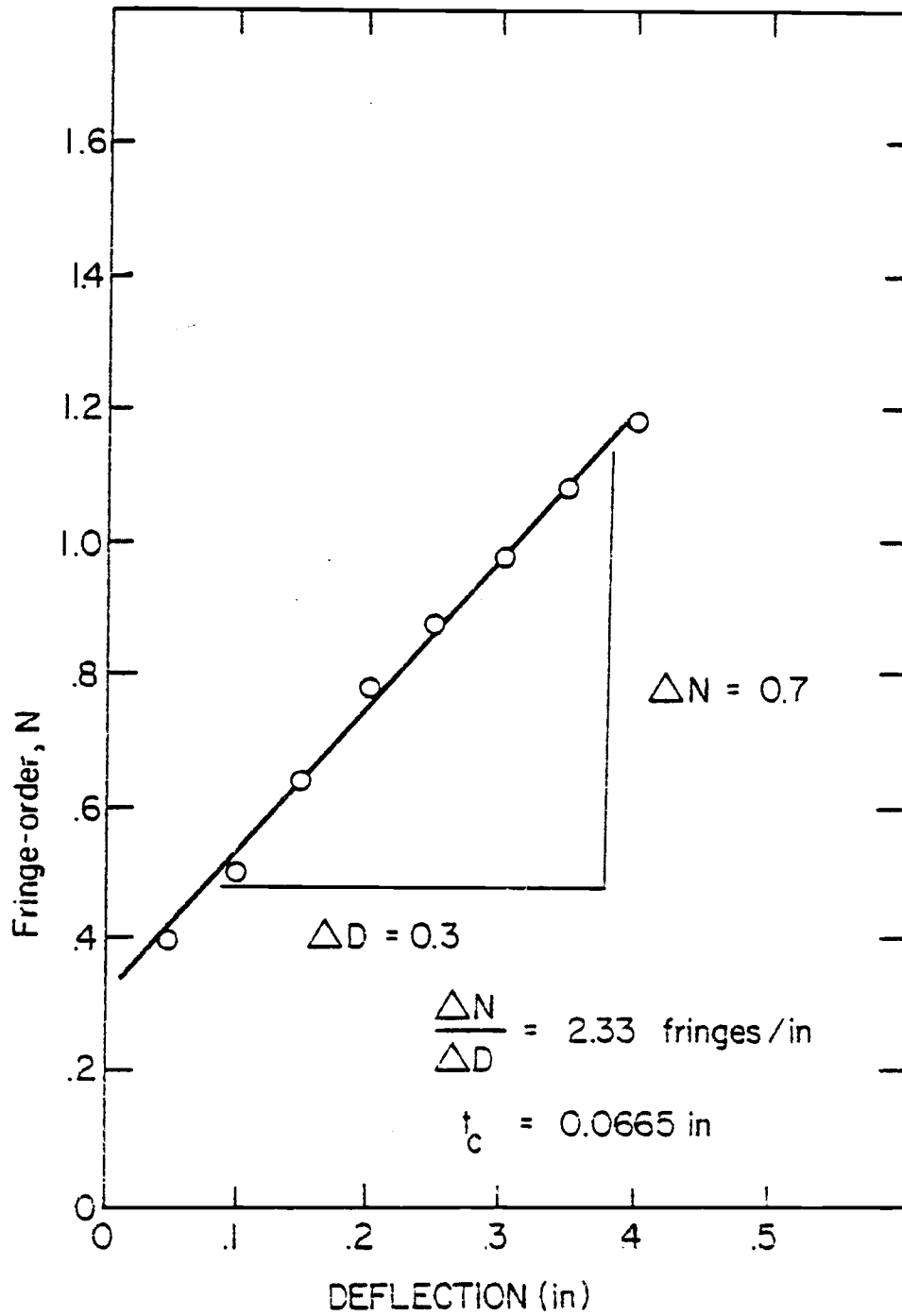


Figure 4.9

PHOTOELASTIC COATING No. 4: Calibration

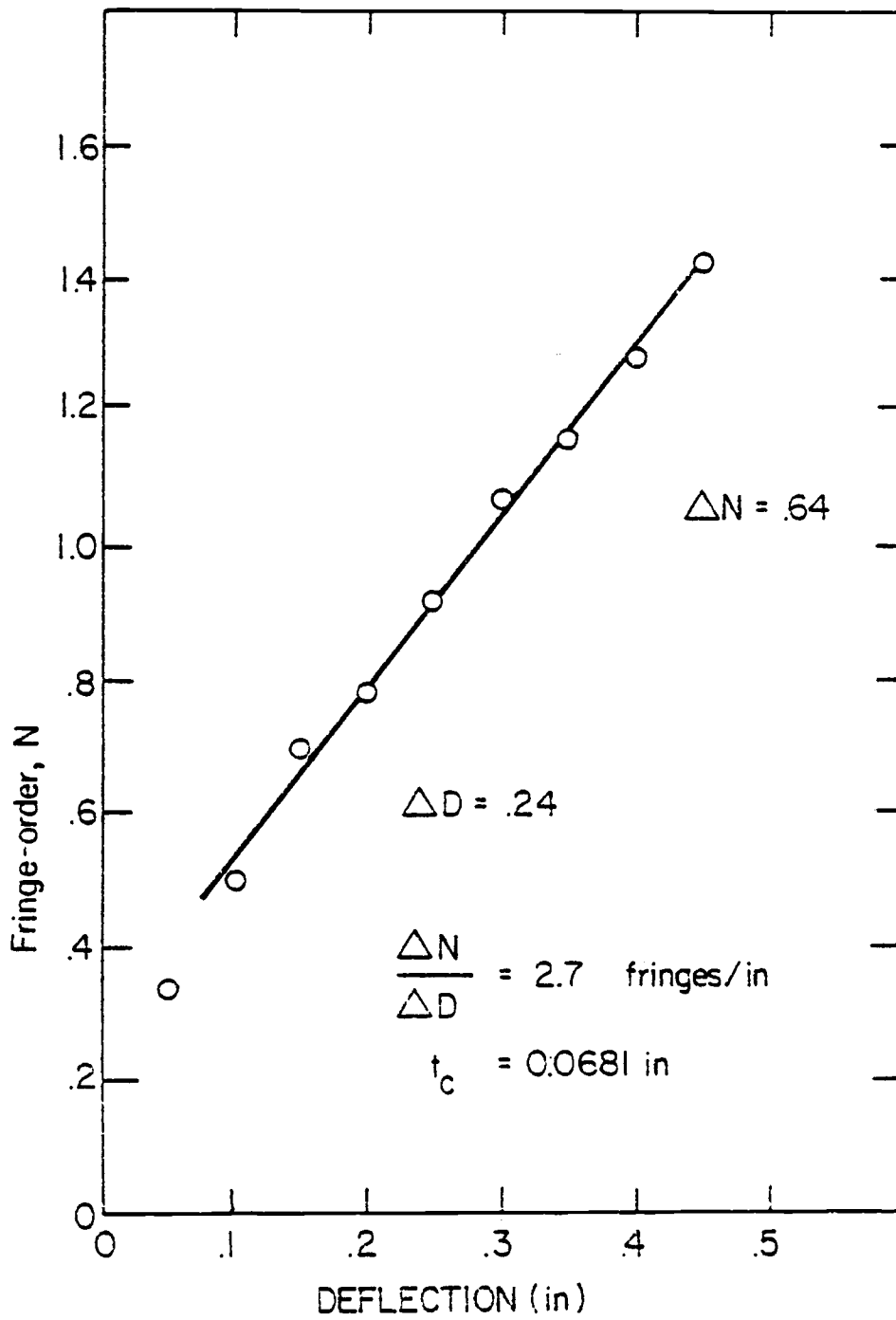


Figure 4.10

Table 4.3

coating	f ($\mu\epsilon$ /fringe)	K (strain-optic coef.)
2	1450	0.0967
3	1800	0.0950
4	1570	0.1050

Based upon a Poisson's ratio of the coating of 0.36 (ref. 11), the following relationships are used to calculate the individual principal strains:

$$\epsilon_x = f(1.5N_\theta - N_n) \quad (4.8)$$

$$\epsilon_y = f(1.5N_\theta - 2N_n) \quad (4.9)$$

where ϵ_x, ϵ_y = principal strains in the directions parallel and perpendicular, resp., to the radial line through knob H when the direction scale is set at zero degrees,

f = fringe value of the coating in $\mu\epsilon$ /fringe,

and N_θ, N_n = fringe orders in oblique and normal incidence, resp. (with correct signs).

The extent to which the separation of principal strains was sought varied from test to test as is seen in the section 4.5 tables. This is due primarily to the difficulty in obtaining the oblique incidence measurements. Also, with the particular geometry of the FCMI simulation model, the necessity of such in-depth work is not a priori. That is to say, sufficient information can be gotten from the normal

incidence measurements, the difference in principal strains, also equal to the shear strain, by simply knowing that little or no axial load is being placed on the apparatus.

Photography was used more extensively for data recording. A small fraction of these are displayed in chapter 5. Each photograph displays a detailed topographical strain map, of the surface strain of the cladding. The isochromatics can be readily identified showing regions of strain gradients and regions of very little stress. Detailed discussion of these are provided in chapter 5.

4.5 Bulk Data Presentation

This section presents, in various forms, the data which provides a basis for discussion and conclusions in chapter 5. The data is shown as follows:

- strain gage results are presented graphically in figures 4.11 to 4.18. They represent strain vs. pump pressure at indicated points on the cladding surface.
- photographic data is presented in chapter 5. Due to "sheer" numbers of slides taken, only a sampling of the 200+ slides are presented. They, however, exhibit the situations and trends found in the various bed types. For comparative considerations,

TEST 3a

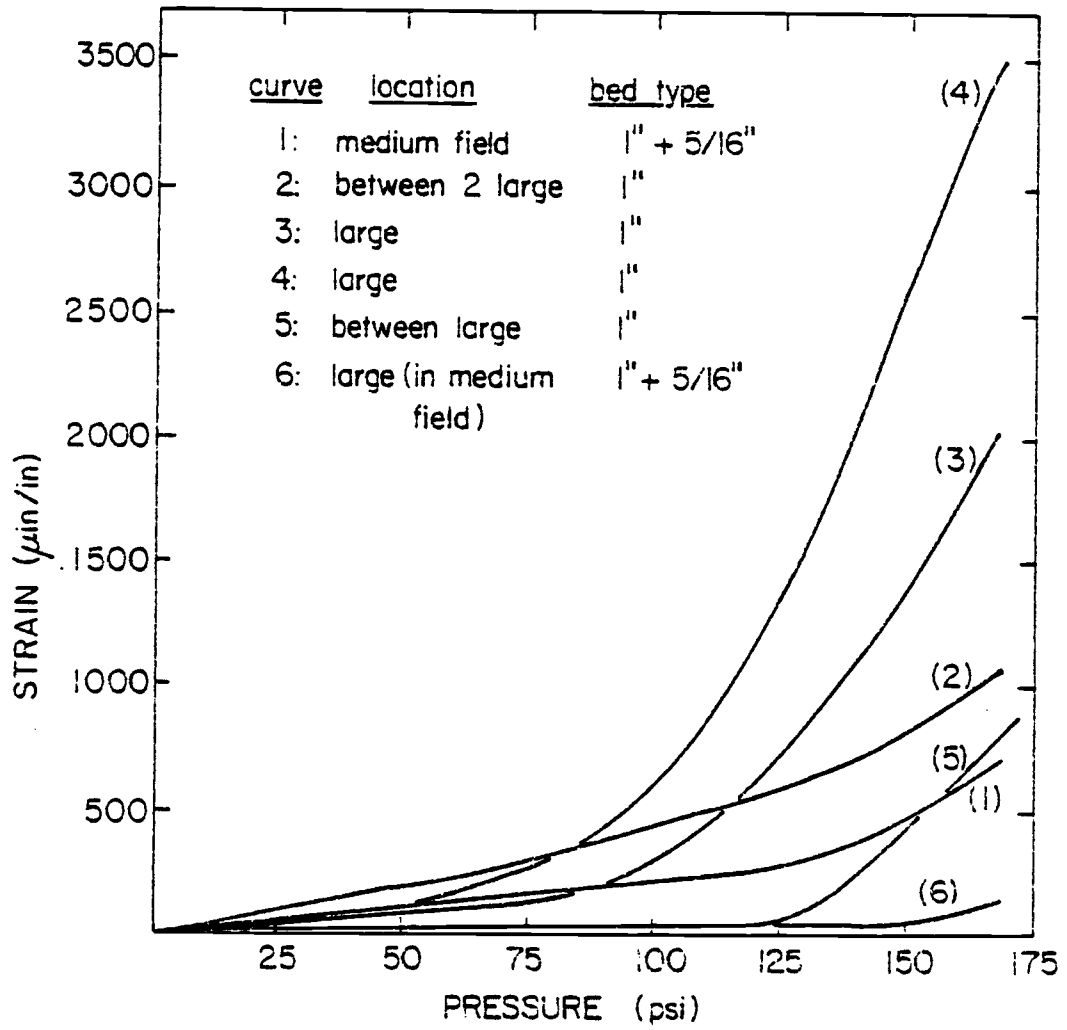


Figure 4.11

TEST 3b

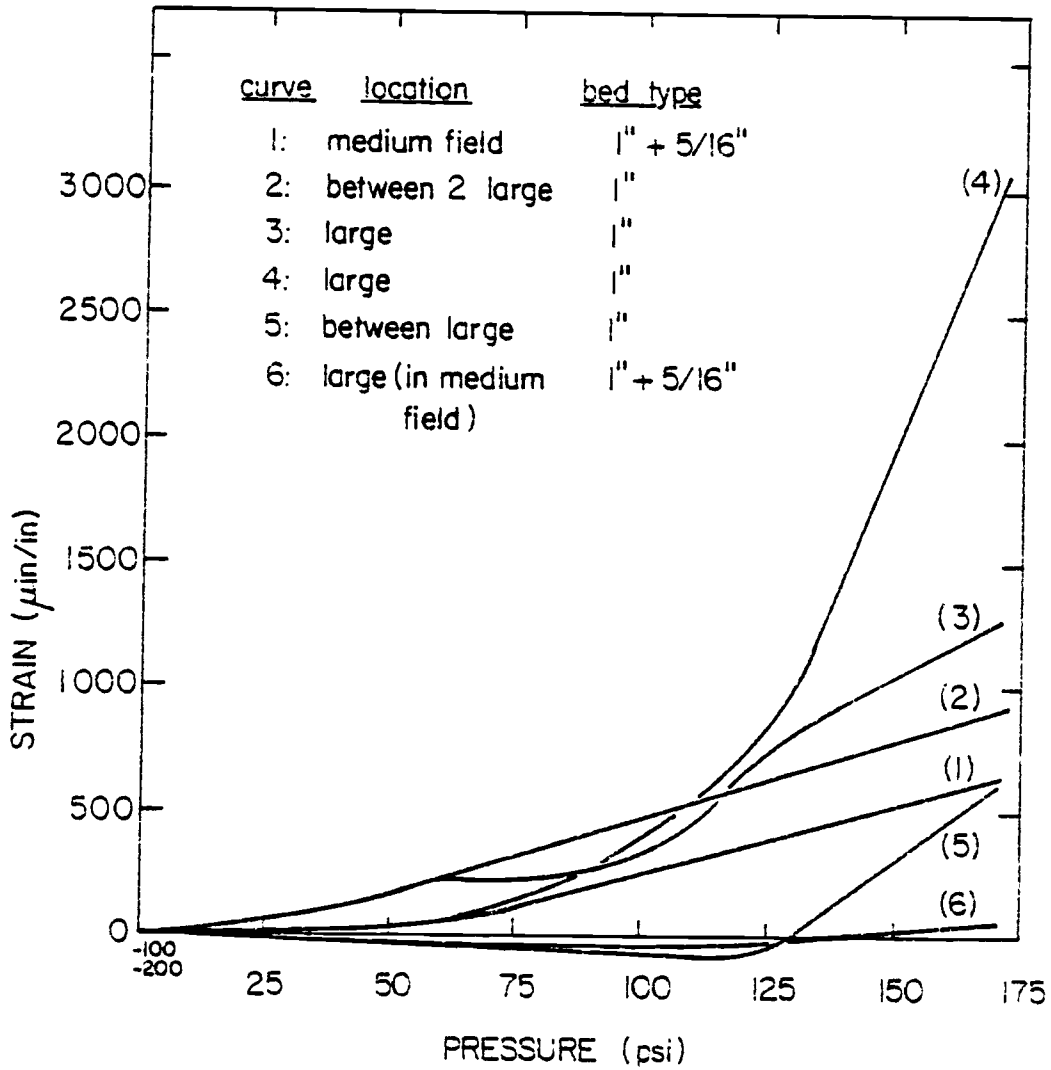


Figure 4,12

TEST 3c

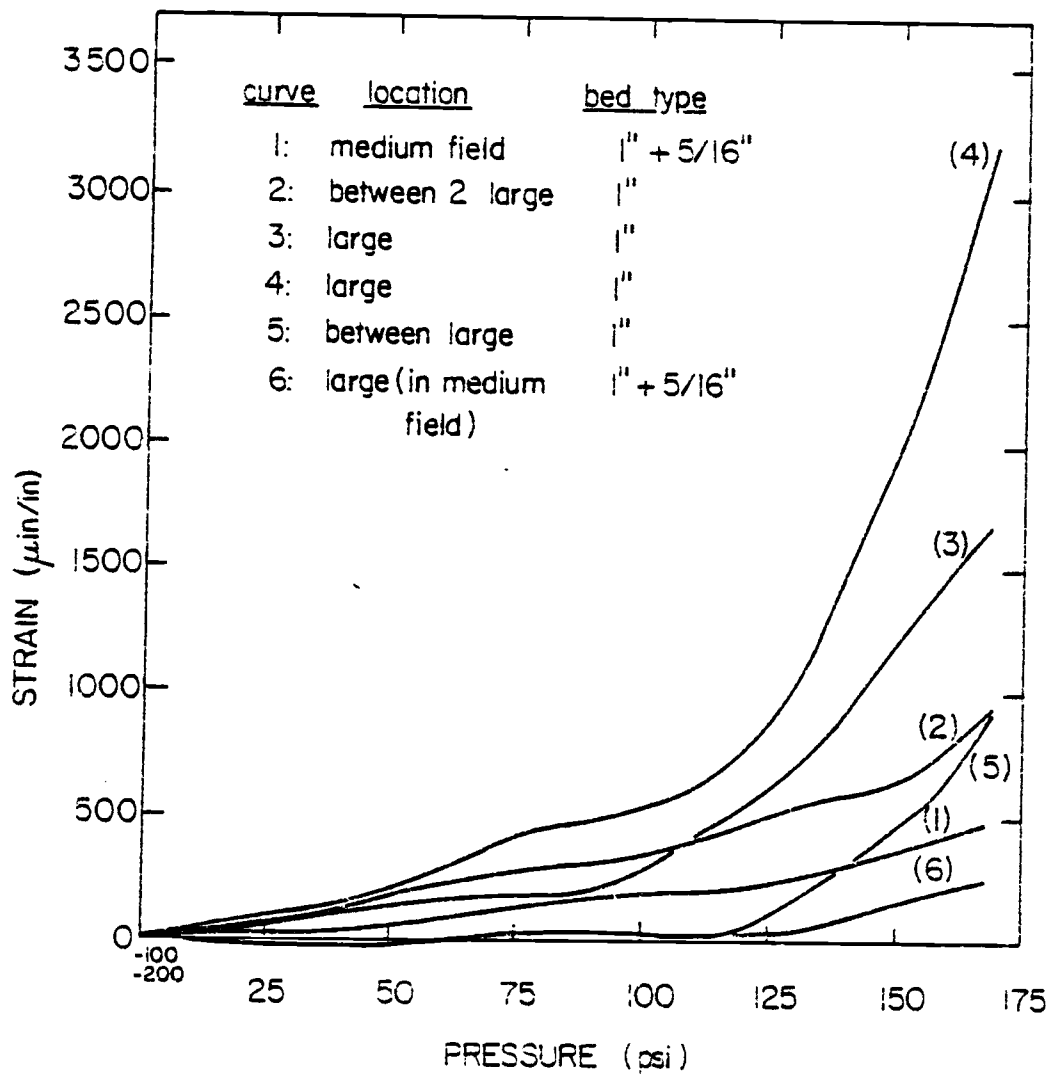


Figure 4.13

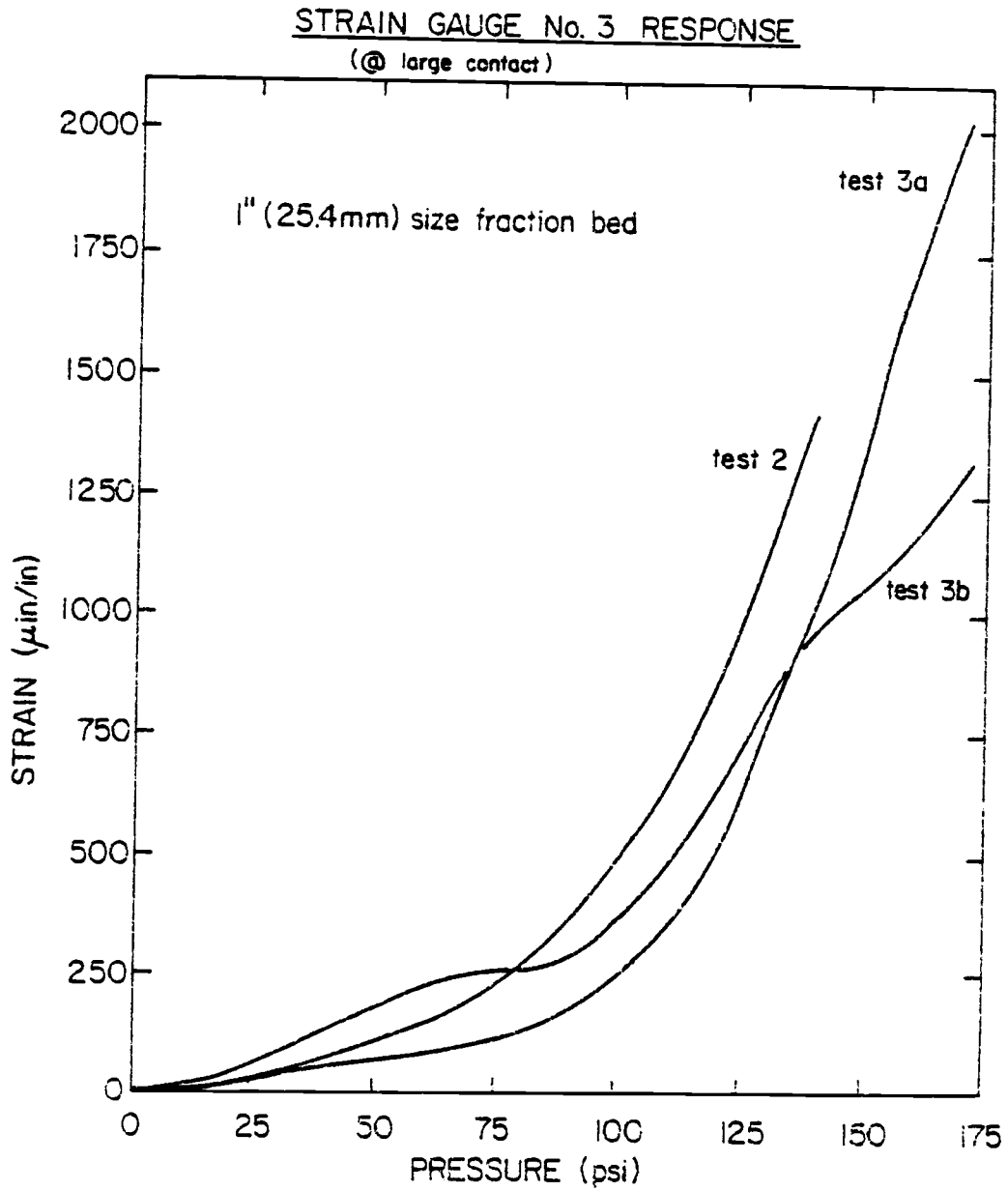


Figure 4.14

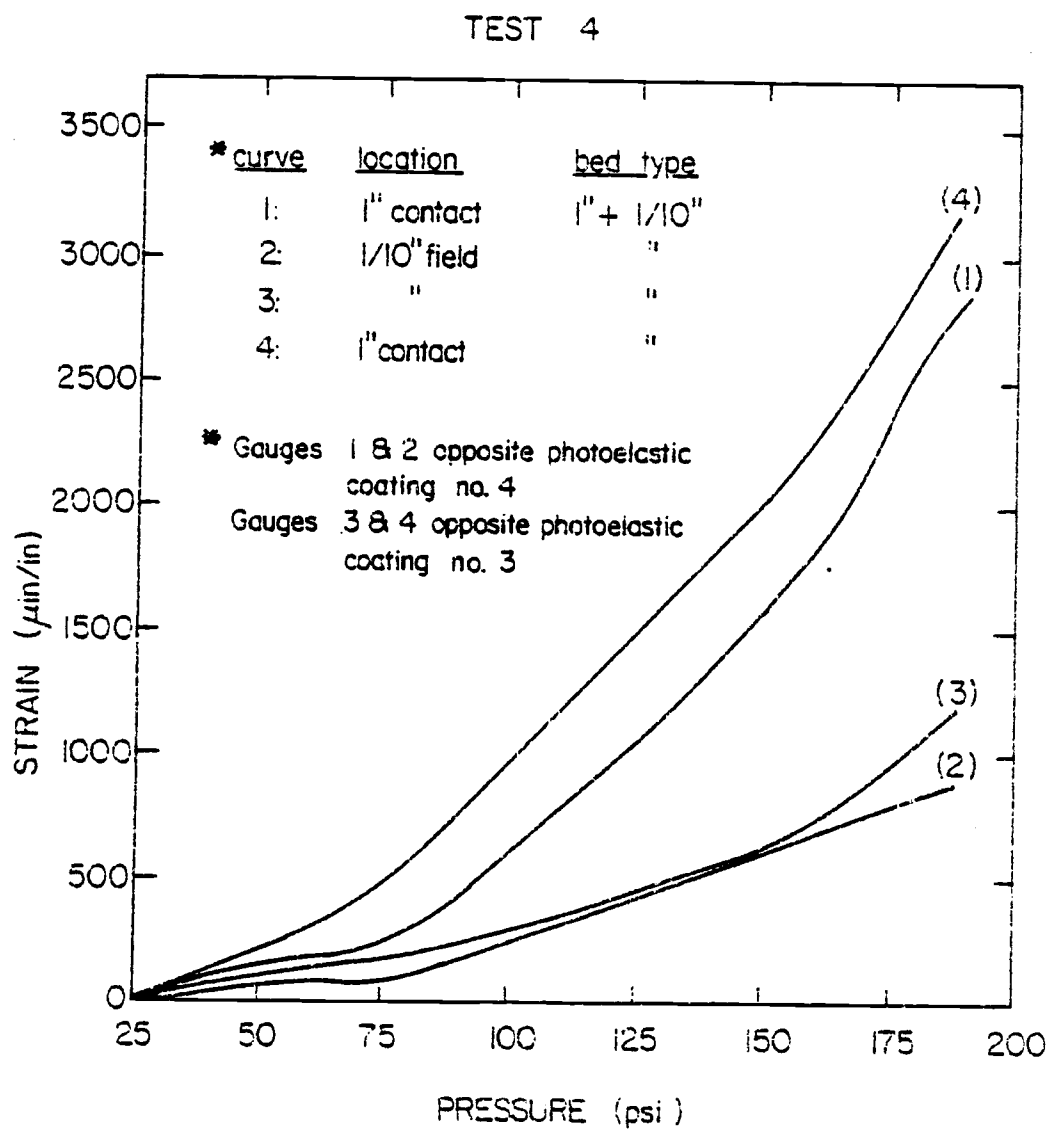


Figure 4.15

TEST 5 (with slide batch 6)

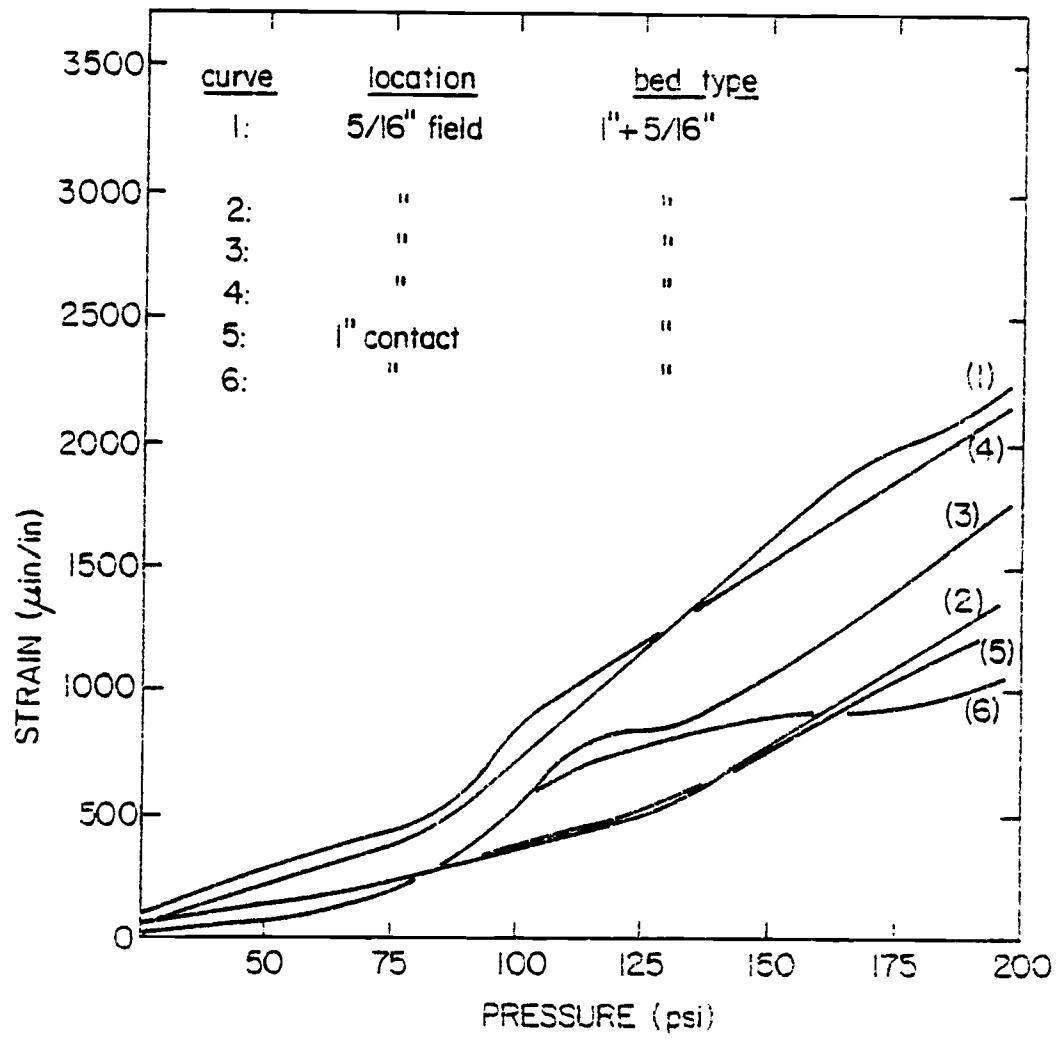


Figure 4.16

TEST 6 (with slide batch 7)

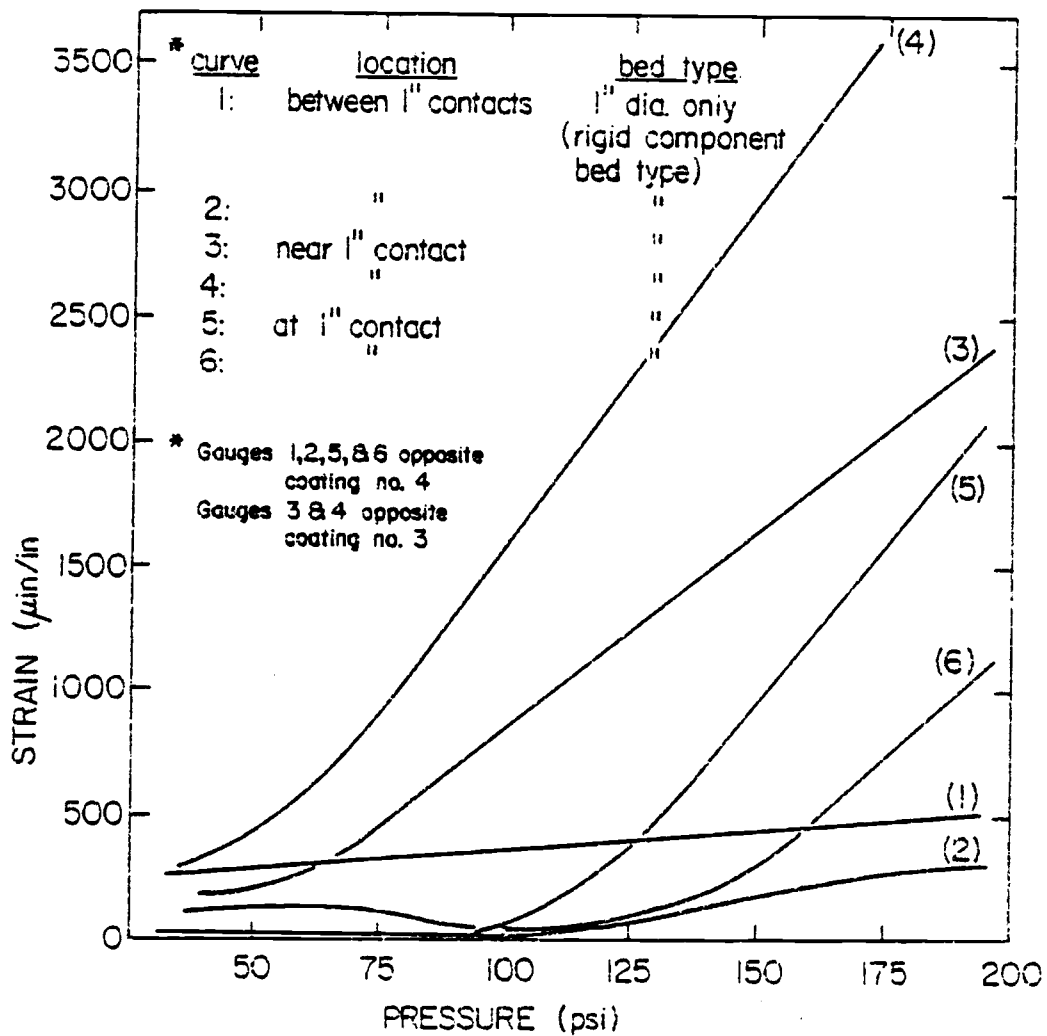


Figure 4.17

TEST 7 (with slide batch 8)

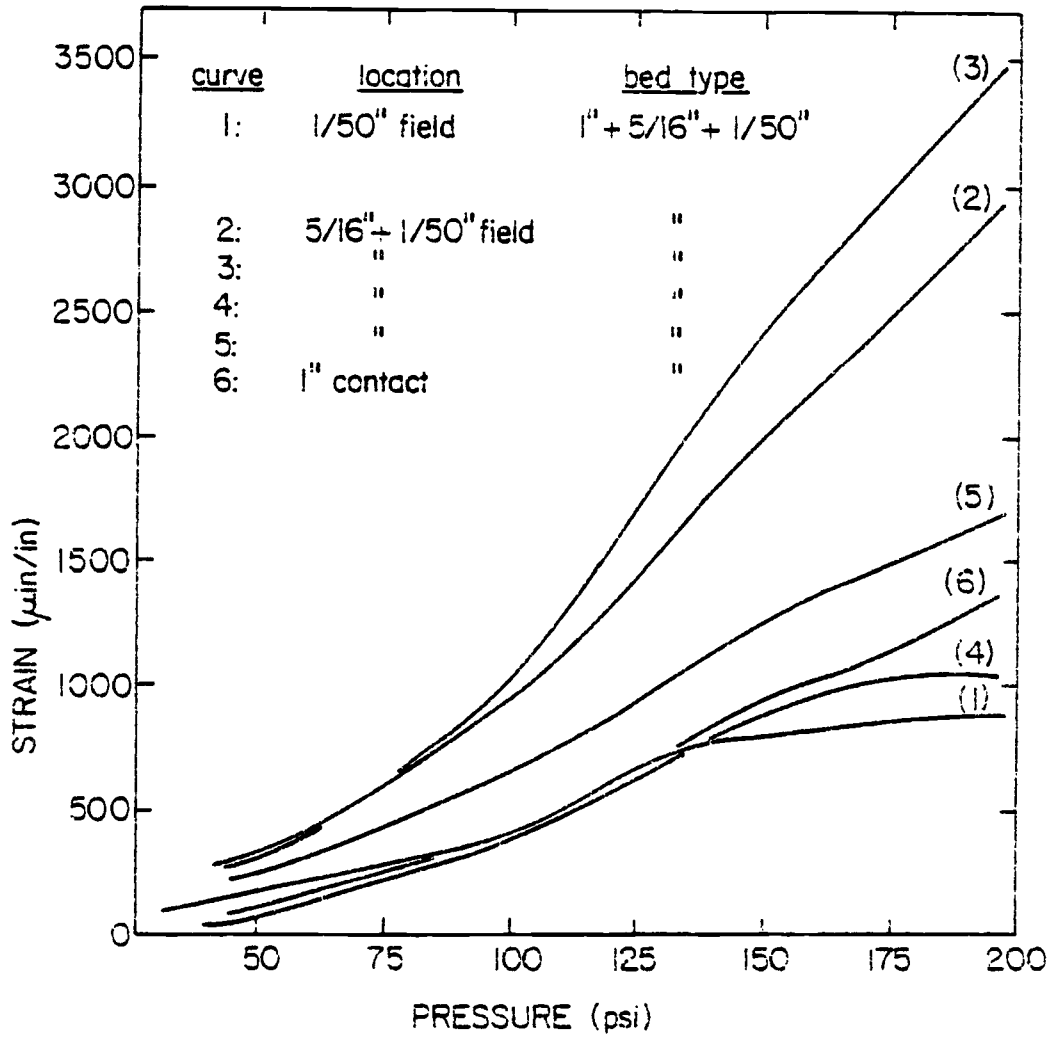


Figure 4.18

all photos are from test pressures of approximately 200 psi.

- the corrected photoelastic coating results are given in tables 4.4 to 4.11. The test which these correspond to is identified. This is the content of section 4.5.1.

4.5.1 Corrected Photoelastic Coating Results

For coating #3: $C = 2.2991$, $f = 1800$

coating #4: $C = 2.3406$, $f = 1570$

The strains are calculated from equations (18) and (19).

For the corrected strains, these equations are simply multiplied by the appropriate correction factor given above.

The resulting form may be expressed as

$$\epsilon_x = C_B f (1.5 N_\theta - N_n)$$

$$\epsilon_y = C_B f (1.5 N_\theta - 2N_n)$$

The following tables give the corrected strains corresponding to the fringe order measurements compiled in the indicated test.

Table 4.4

(Coating #3)

P = 200 psi, 1" + 1/10", Batch 2

<u>point</u>	<u>ϵ_x</u>	<u>ϵ_y</u>
1	-827	1572
2	-	-
3	-766	2752
4	-373	3476
5	1200	5007
6	-	-
7	-827	4428
8	-	-

Table 4.5

(coating #4)

P = 200 psi, 1" + 1/10", Batch 2

<u>point</u>	<u>ϵ_x</u>	<u>ϵ_y</u>
1	-182	3381
2	-1360	3785
3	-735	2940
4	-1249	1911
5	-	-
6	-	-
7	-	-
8	-	-

Table 4.6
(coating #3)

1" + 5/16", Batch 5
P = 170 psi

<u>point</u>	<u>ϵ_x</u>	<u>ϵ_y</u>
1	1510	4945
2	-21	3455
3	-537	2028
4	413	4552
5	-206	3931
6	579	2897
7	1862	4966
8	579	5876

Table 4.7
(coating #3)

P = 210 psi

<u>Point</u>	<u>ϵ_x</u>	<u>ϵ_y</u>
1	-1874	5181
2	-	-
3	-1653	3968
4	-845	5695
5	-	-
6	-1322	3527
7	-1028	3895
8	587	4483

Table 4.8

(approximate maximum values)

(1" + 5/16")

<u>coating</u>	<u>ϵ_x</u>	<u>ϵ_y</u>
3	496	7055
4	-367	5328

Table 4.9

(approximate maximum values)

(1" only)

<u>pressure</u>	<u>coating</u>	<u>ϵ_{\max}</u>	
170	3	-703	3931
170	4	-1616	2278
200	3	-	-
200	4	-	-

Table 4.10
(coating #3)

(LWR, Batch 8)

<u>point</u>	<u>ϵ_x</u>	<u>ϵ_y</u>
P = 150 psi		
1	993	2731
2	2151	4303
3	662	3310
4	1158	5297
P = 200 psi		
1	786	3683
2	2234	5214
3	331	3765
4	-910	4386

Table 4.11

(coating #4)

(LWR, Batch 8)

<u>point</u>	<u>ϵ_x</u>	<u>ϵ_y</u>
P = 150 psi		
1	-220	1763
2	310	3786
3	587	1727
4	532	2553
P = 200 psi		
1	-587	2131
2	514	5107
3	110	1874
4	-146	3013

Chapter 5: Analysis and Discussion of Results

In drawing conclusions from the data presented in chapter 4, it is helpful first to explore the situation analytically. Comparisons between experimental results and the predicted stress-strain response from these calculations may provide insight into the mechanisms at work in the mechanical interaction between a sphere pac bed and a cladding wall.

The analytic approaches are developed in sections 5.1.1 to 5.1.4. Section 5.2 then lists the physical results and discusses the comparisons with the calculational models.

5.1 Comparative Analysis

Several approaches may be taken to model the situation analytically. Hoop stress is the desired parameter. From the experimental data, approximations may be made for average tangential strain values by simple averaging of local strains. Strain gage and photoelastic data provide these local values for comparison.

5.1.1

The situation may be modeled either simply or in very complex detail. In the simplest case, the acrylic cladding may be considered a thin walled pressure vessel and the internals (bladder and simulated fuel) an incompressible fluid. In this case, pressure loss is neglected through the

hose, sphere pac bed and cladding. The strain approximation may then be expressed (ref. 17) as

$$\epsilon_t = \frac{\sigma_t}{E} = pr/Et \quad (5.1)$$

where ϵ_t = hoop strain

p = internal pressure

r = cladding radius (average)

t = cladding thickness.

For a pressure of 200 psi,

$$= 11347 \text{ } \mu\text{in/in}$$

As an average value, this is very high compared to actual experimental results. This suggests a modification is necessary.

5.1.2

A modified approach is to continue modeling the fuel region as an incompressible fluid, but do not neglect the pressure loss through the expansion hose. To do this, elastic properties of the hose are necessary. From figure 4.1, the modulus of elasticity may be estimated. From the curve;

$$\begin{aligned} E &= (130\text{psi})(4.5\text{in})/(0.1333\text{in}) \\ &= 4680\text{psi} \end{aligned}$$

As rubber is nearly incompressible, a Poisson's ratio may be approximated as near the maximum of 0.5. A value of

$$\nu = 0.4$$

was chosen as a representative value.

The method of approach is to consider the general case of elastic stresses in thick-walled cylinders. The governing equation for this situation (ref. 18) is

$$\frac{\sigma_t - \sigma_r}{r} - \frac{d\sigma_r}{dr} - \beta = 0 \quad (5.2)$$

where r = radius

σ_t = tangential stress

σ_r = radial stress

β = body force.

It can be shown that for an incompressible fluid in the absence of the body force, β ,

$$\frac{d\sigma_r}{dr} = 0$$

Therefore, at any point within the "fluid," $\sigma_r = \sigma_t$.

Further relationships involved in this modeling are developed at the cylinder interfaces. At the hose outer surface, r_b , the radial displacement is given by

$$\delta_b = \epsilon_{tb} r \quad (5.3)$$

where ϵ_{tb} = tangential strain.

From the biaxial Hookes' law, one has the relationship between biaxial stress and strain as

$$\delta_b = r_b \varepsilon_{t_b} = \frac{r_b}{E_{ab}} (\sigma_{t_b} - \nu_{ab} \sigma_{r_b}) \quad (5.4)$$

Similarly, for the acrylic cladding inner surface,

$$\delta_c = r_c \varepsilon_{t_c} = \frac{r_c}{E_{cd}} (\sigma_{t_c} - \nu_{cd} \sigma_{r_t}) \quad (5.5)$$

From conservation of areas,

$$\delta_b r_b = \delta_c r_c \quad (5.6)$$

For the rubber bladder and the acrylic cladding, the solution of eq. (5.2) gives the values of the tangential stress (ref. 18) as

$$\sigma_{t_b} = \frac{p_a r_a^2 - p_b r_b^2}{r_b^2 - r_a^2} + \frac{(p_a - p_b) r_b^2 r_a^2}{(r_b^2 - r_a^2) r_b^2} \quad (5.7)$$

$$\sigma_{t_c} = \frac{p_a r_c^2 - p_d r_d^2}{r_d^2 - r_a^2} + \frac{(p_c - p_d) r_d^2 r_c^2}{(r_d^2 - r_c^2) r_c^2} \quad (5.8)$$

In these equations, both p_a and p_b are known values.

Equations (5.4) through (5.8) provide five equations in the 5 unknowns;

$$\sigma_{t_b}, \sigma_{t_c}, \sigma_r, \delta_b, \delta_c$$

The quantity σ_r from the incompressible fluid approximation of the simulated fuel region takes on the values

$$\sigma_r = -p_a = -p_b \quad (5.9)$$

Simultaneous solution of these equations gives an internal pressure in the fuel region as

$$p_b = \frac{r_b B}{Cr_c - Ar_b} \quad (5.10)$$

where

$$A = \frac{-rb}{E_{ab}} \left(\frac{r_b^2 + r_a^2 - \nu_{ab}(r_b^2 - r_a^2)}{r_b^2 - r_a^2} \right) \quad (5.11)$$

$$B = \frac{r_b}{E_{ab}} \left(\frac{2p_a r_a^2}{r_b^2 - r_a^2} \right) \quad (5.12)$$

$$C = \frac{r_c}{E_{cd}} \left(\frac{r_c^2 + r_d^2 - \nu_{cd}(r_d^2 - r_c^2)}{r_d^2 - r_c^2} \right) \quad (5.13)$$

To approximate the tangential strain at the cladding surface, this value of pressure (eq. 31) is substituted into the thin-walled pressure vessel approximation as

$$\epsilon_t = p_b r_d / E_{cd} t \quad (5.14)$$

where the constants have the values

$$r_d = 5 \text{ in, } t = 3/16 \text{ in,}$$

$$\text{and } E_{cd} = 0.47 \times 10^6 \text{ psi}$$

The results are presented in table 5.1.

Table 5.1

<u>pump pressure (psi)</u>	<u>p</u>	<u>ϵ_{τ}</u>
0	0	0
40	34.4	1952
60	51.6	2928
80	68.8	3903
100	86.0	4879
120	103.2	5855
140	120.4	6808
160	137.6	7807
180	154.8	8783
200	172.0	9795
210	180.6	10247

As in the previous approximation (sect. 5.1.1) the strain predictions far exceed even the maximum strain values determined experimentally in any of the tests.

5.1.3 Rock Mechanics Solution

Again, the problem is to determine the pressure on the acrylic cladding given the internal hose pressure as read by the gage (see chap. 2).

Treat the steel balls (simulated fuel) as a cohesionless granular medium. Consider the fuel and tube separately. Assume the fuel is fully plastic (i.e. yielded) and obeys the Mohr-Coulomb yield criterion (ref. 19, 20,

21). Assuming plane strain ($\epsilon_z = 0$) the Mohr-Coulomb criterion may be expressed as

$$f = \sigma_r - N\sigma_t = 0 \quad (5.15)$$

where
$$N = \frac{1 + \sin\phi}{1 - \sin\phi}$$

ϕ = angle of internal friction.

From equation (5.15) one has that

$$\sigma_t = \sigma_r/N \quad (5.16)$$

Substituting this into the equilibrium equation

$$\frac{\sigma_r - \sigma_t}{r} + \frac{d\sigma_r}{r} = 0 \quad (5.17)$$

yields

$$\frac{d\sigma_r}{dr} + \frac{N-1}{N} \frac{\sigma_r}{r} = 0 \quad (5.18)$$

The solution to eq. (5.18) is given by

$$\sigma_r = Cr^{-\left(\frac{N-1}{N}\right)} \quad (5.19)$$

where C is an arbitrary constant. This constant is determined from the boundary condition

$$\sigma_r = p_i \text{ at } r = a \quad (5.20)$$

therefore

$$C = p_i a^{\left(\frac{N-1}{N}\right)} \quad (5.21)$$

$$\text{thus } \sigma_r = p_i (r/a)^{-\left(\frac{N-1}{N}\right)} \quad (5.22)$$

One also has that

$$\sigma_r = p_o \text{ at } r = b$$

therefore

$$p_o = p_i (b/a)^{-\left(\frac{N-1}{N}\right)} \quad (5.23)$$

$$\text{or } p_o/p_i = (b/a)^{-\left(\frac{N-1}{N}\right)} \quad (5.24)$$

Numerical results

For $a = 2.25$ in.

$b = 5.0$ in.

ϕ depends on the type of fuel (ref. 22).

- for steel balls alone;

$$\phi = 14 \text{ thus } N = 1.64$$

- for steel and alumina;

$$\phi = 27 \text{ thus } N = 2.66$$

thus, - for steel balls alone;

$$p_o/p_i = 0.7323$$

- for steel and alumina;

$$p_o/p_i = 0.6076$$

Approximating p_i , the pressure at the outer surface of the rubber hose, can be done using the derivation of section

5.1.2. The values obtained in this approach are shown in tables 5.2 and 5.3.

Table 5.2
(steel balls only)

<u>P</u> (psi)	<u>P_i</u>	<u>P_o</u>	<u>μin/in</u>
100	86	63	3574
140	120	88	4909
180	155	113	6303
200	172	126	7029

Table 5.3
(steel plus alumina)

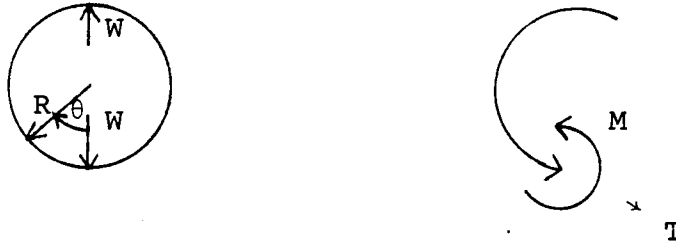
<u>P</u> (psi)	<u>P_i</u>	<u>P_o</u>	<u>μin/in</u>
100	86	52	2900
140	120	72	4016
180	155	93	5188
200	172	103	5746

5.1.4 Local Stress in Cladding Due To Spheres

The previous calculations (sections 5.1.1 to 5.1.3) have dealt with hoop stress or strain. It is desirable to obtain approximations regarding strain levels due to point

loading; namely, the sphere contact loads found in a sphere pac fuel pin type situation.

To accomplish this, consider two concentrated forces on a ring;



From (ref. 23) the solution is

$$T = 0.5W|\sin\theta| \quad (5.25)$$

$$M = WR(1/\pi - 0.5|\sin\theta|) \quad (5.26)$$

for a thin ring,

$$\sigma = \frac{Mc}{I} + \frac{T}{A} \quad (5.27)$$

The case of many spheres pressing against the cladding may be approximated as $2N$ equally spaced, concentrated forces acting on a ring. Using the above solution and superposition, one has

$$T = 0.5W \sum_{j=1}^N [\sin(\theta - (j-1)\pi/N)] \quad (5.28)$$

$$M = \frac{NWR}{\pi} - 0.5WR \sum_{j=1}^N |\sin(\theta - (j-1)\pi/N)| \quad (5.29)$$

For stress on the ring at a sphere contact point, $\theta = 0$ and

$$T = 0.5W \sum_{j=1}^N \sin(j-1)\pi/N \quad (5.30)$$

$$M = \frac{NWR}{\pi} - 0.5WR \sum_{j=1}^N \sin(j-1)\pi/N \quad (5.31)$$

which simplifies to

$$T = 0.5W \frac{\cos\pi/N}{\sin\pi/2N} \sin(N+1) \frac{\pi}{2N} - 2\cos \frac{\pi}{2N} \cos(N+1) \frac{\pi}{2N} \quad (5.32)$$

$$M = \frac{NWR}{\pi} - 0.5WR \frac{\cos\pi/N}{\sin\pi/2N} \sin(N+1) \frac{\pi}{2N} - 2\cos \frac{\pi}{2N} \cos(N+1) \frac{\pi}{2N} \quad (5.33)$$

For $A = t$, $I = t^3/12$, and $c = t/2$

from equation (5.27)

$$\sigma = W \frac{6NR}{\pi t} + \frac{1}{2} \left(1 - \frac{6R}{t}\right) \frac{\cos\pi/N}{\sin\pi/2N} \sin \frac{\pi(N+1)}{2N} - 2\cos \frac{\pi}{2N} \cos \frac{\pi(N+1)}{2N} \quad (5.34)$$

For stress on the ring at a location between two spheres,

$$\theta = \pi/2N$$

therefore

$$T = 0.5W(\cot\pi/2N \sin\pi(N+1)/2N - \cos\pi(N+1)/2N) \quad (5.35)$$

$$M = \frac{NWR}{\pi} - 0.5WR(\cot \frac{\pi}{2N} \sin \frac{\pi(N+1)}{2N})$$

and

$$- \cos \frac{\pi(N+1)}{2N} \quad (5.36)$$

$$\sigma = \frac{W}{t} \left\{ \frac{6NR}{\pi t} + \frac{1}{2} \left(1 - \frac{6R}{t} \right) \left(\cot \frac{\pi}{2N} \sin \frac{\pi(N+1)}{2N} - \cos \frac{\pi(N+1)}{2N} \right) \right\} \quad (5.37)$$

For N very large (i.e. many small spheres)

$$\sigma \cong \frac{WN}{\pi t} \quad (5.38)$$

Consider the case where R = 5.0 in., t = 0.2 in., and sphere radius = 0.5 in., then N = 14

-- at sphere, $\sigma = 36W$

-- between spheres, $\sigma = 15W$

-- many spheres, $\sigma = 22W$

5.2 Results

From both strain gage and photoelastic coating results, typical hoop strain values were found to be in the range of approximately 2000 to 4000 micro-strain at a pressure level of 200 psi (pump pressure). These values however represent averaged strains from, in most tests, six gages on the cladding surface. In the photoelastic coating situations, generally eight points were used in which the principal strains were determined.

The photoelastic results gave higher strain values than the gages, but not unexpectedly. All gages were mounted to measure normal strain in the θ direction whereas photostress methods are capable of yielding the actual minima and maxima

which are not necessarily in directions absolutely perpendicular to the axis of expansion.

The strain gage plots (figures 4.11 to 4.18) demonstrate an important point; namely that the stress distribution arising from the expanding bed of spheres is very non-uniform. Rather than all spheres feeling and transmitting similar loads, they transmit loads which reflect very erratic packing situations. For instance, from fig. 4.12 compressive regions of the cladding are seen. From most all strain plots, it is obvious that great disparities exist in load transmission magnitudes. In other cases, strain ranges were narrower, for example fig. 4.15 where the strains were found to be ranging from 1000 to 2500 micro-strain at 200 psi.

The strain gage information is, however, very limited in application due to the very statistical nature of the beast. The importance of the strain gages in this study came in two areas; (1) to supply input to preliminary calculations for photoelastic coating preparation, and (2) for comparative strain values given coating strain results. As mentioned above, favorable comparison was achieved in that magnitudes and directions of strain vectors were of the same order.

The bulk of the useful information was provided in the photoelastic coating data. The information is very qualitative overall, but also quantitative in relative

studies of the bed types. The discussion of these results will proceed in four parts; one for each bed type examined. Following this, conclusions will be discussed in section 5.3.

-- Coarse fraction only (see figures 5.1 and 5.2)

This bed type simulation consists of the non-infiltrating component of the LMFBR fuel type. The sphere matrix for this simulation generally appeared very regular in its packing configuration. As shown in table 2.2, the packing factor for this type was approximately 60% comparing very favorably to that of (U,Pu)C fuel type. The surface density of contact points per square area was slightly greater than 1 per square inch.

Referring to figures 5.1 and 5.2, approximately 15 contact points are apparent, giving a load transmission fraction of near 20-25%; of these, yet, only a select few transmit a load that is substantial in comparison to the 15. The remainder of the transmitting spheres give rise to only a nominal fringe order gradient in their vicinity.

For the few transmitting spheres, gradients were seen on the order of 1.5 fringes/0.5 in. The locations of the transmitting spheres appeared random. The stress in the vicinity of these points appeared affected only by the one contact. Other contacts were generally not discernible within a 3-4 in. radius. Peripheral to this region, points were visible but again with only nominal gradients.



Figure 5.1. Coarse fraction simulation.

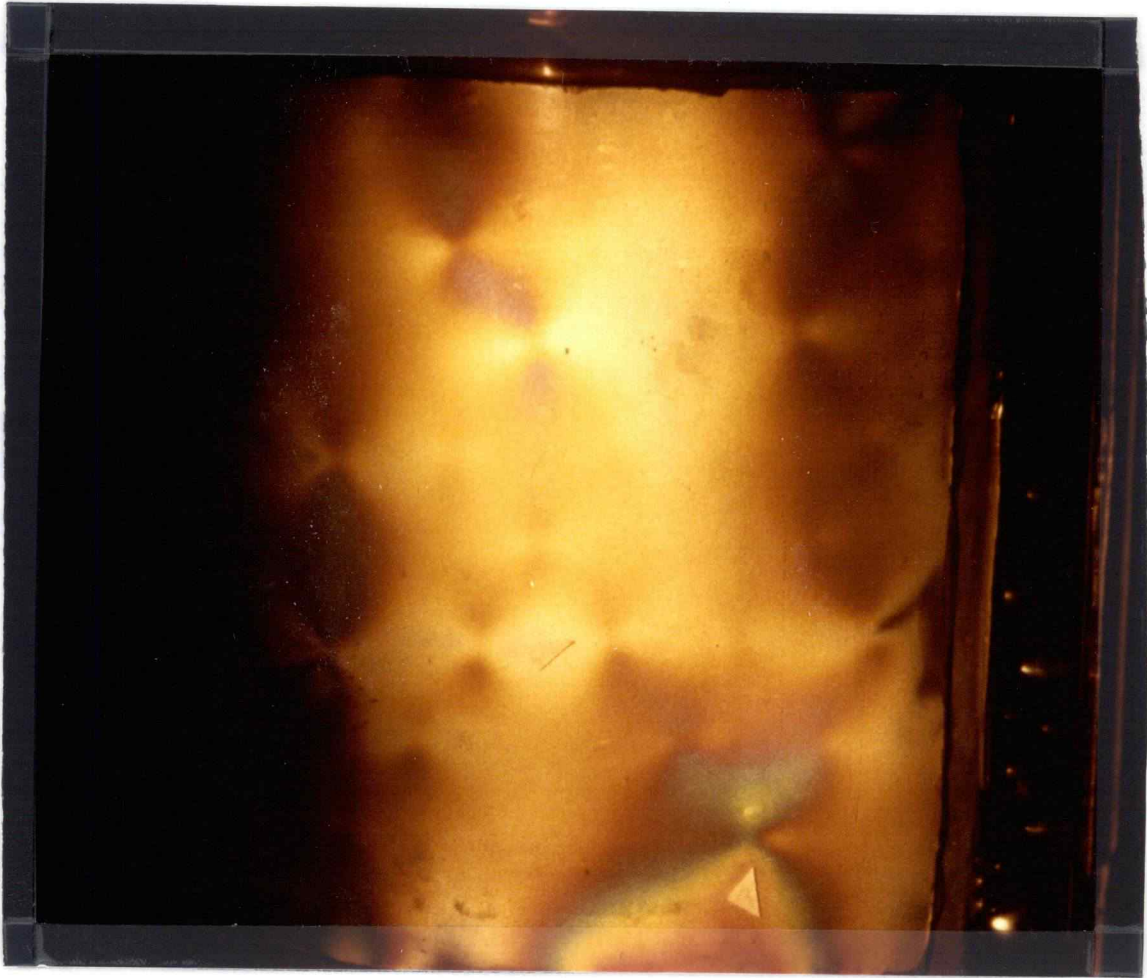


Figure 5.2. Coarse fraction simulation.

-- Coarse plus fine fraction (LMFBR combination, figures 5.3 and 5.4)

As in the above case, the matrix was quite uniform at the cladding inner surface. The coarse fraction contact point density was near one per square inch. The packing factors again compare very favorably (refer to table 2.2).

The resulting stress-strain distribution in the cladding was quite uniform in comparison to the coarse fraction bed alone. Gradients were still present but generally were less than 0.6 fringes per inch. Visible contact points numbered close to 40-50%, a large increase over the coarse bed. The contact point spacing was also very uniform, i.e. approximately 1.5 in. spacing.

The principal stress axes were very nearly perpendicular at all points (to within a 5-10 degree variation).

-- Coarse plus medium (figures 5.5 and 5.6)

This bed type simulation consists of the two non-infiltrating components of the three-size-fraction, light water reactor fuel. The packing factors achieved compared favorably to those used in actual practice (table 2.2).

Uniformity in the sphere matrix at the cladding inner surface was not nearly so evident as in the previous two cases. This bed type is very sensitive to a given loading

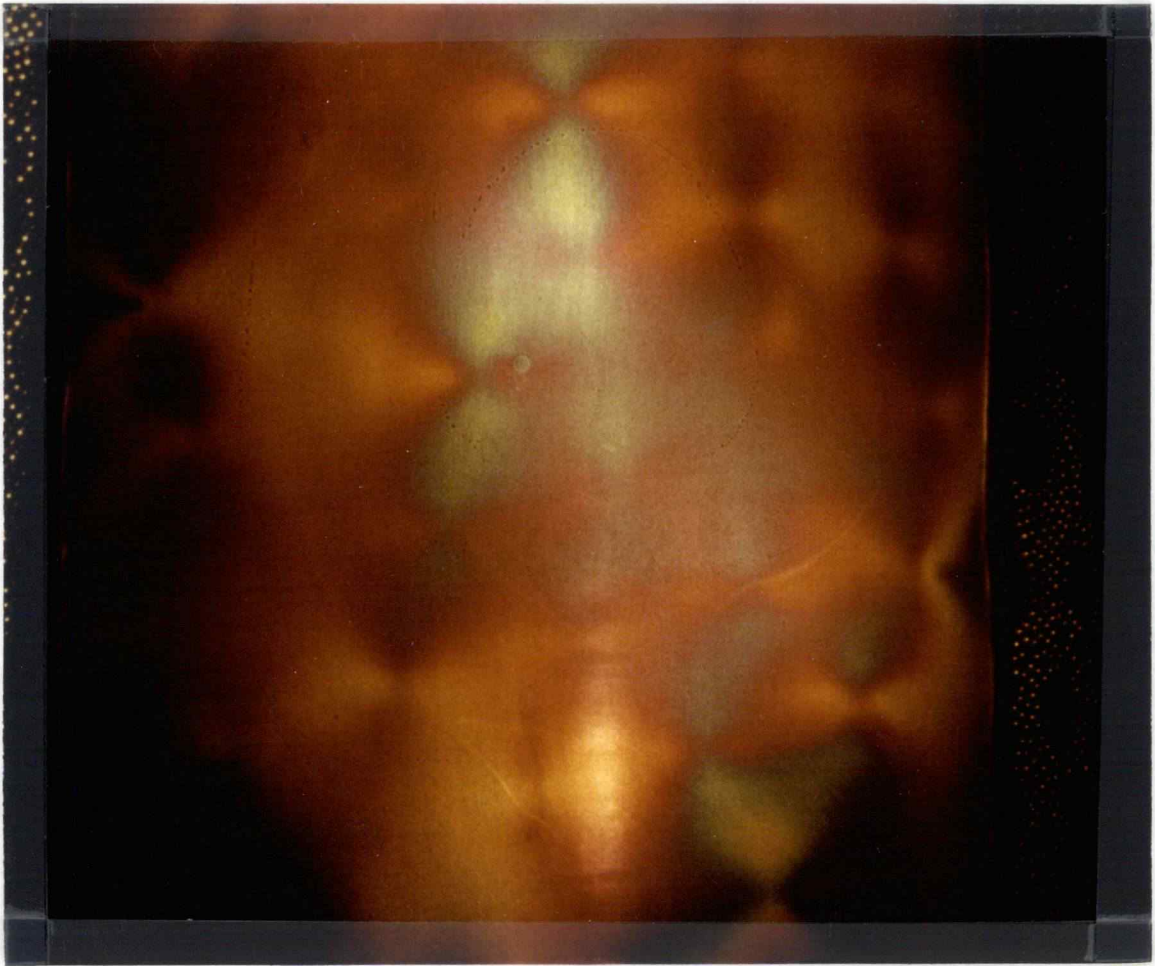


Figure 5.3. Coarse plus fine simulation.
(LMFBR combination)

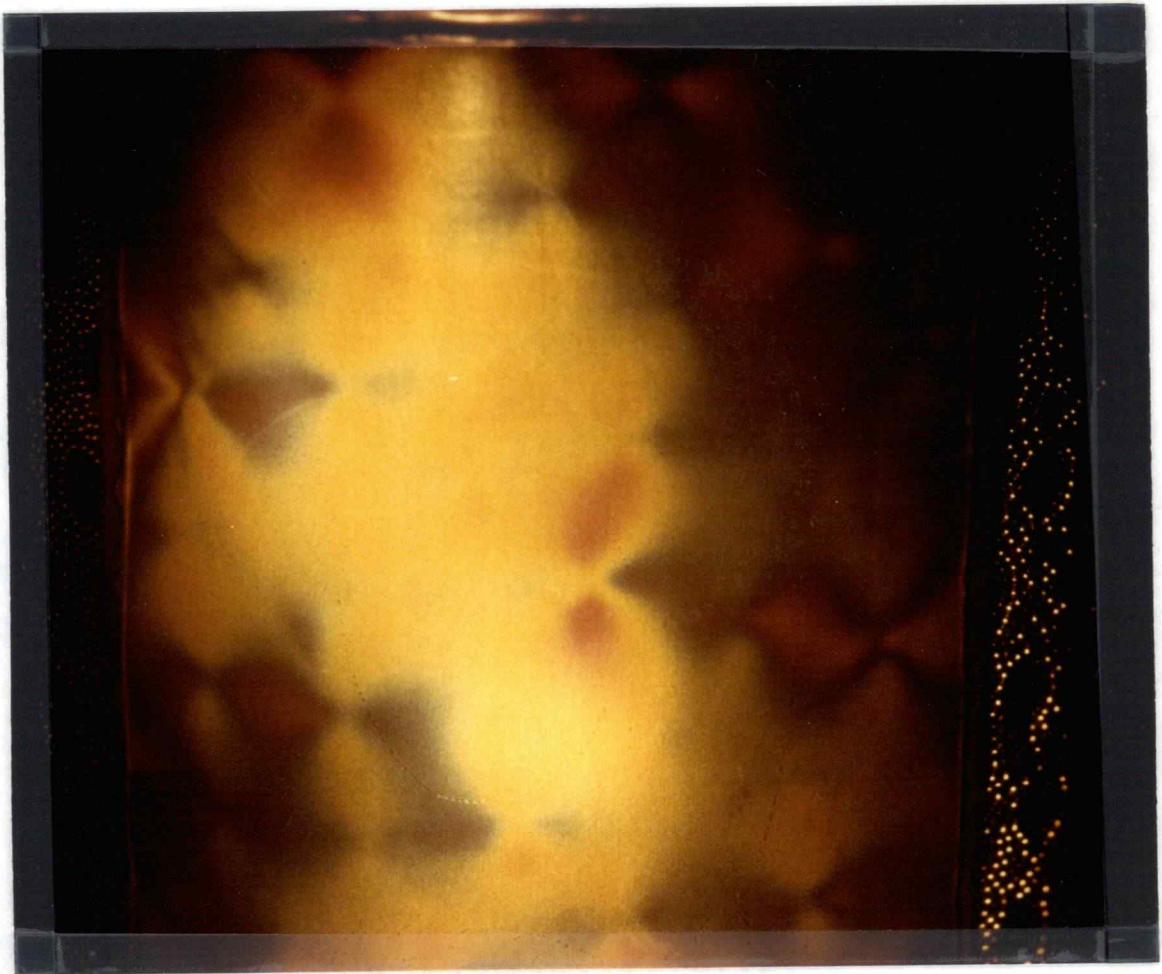


Figure 5.4. Coarse plus fine simulation.
(LMFBR combination)

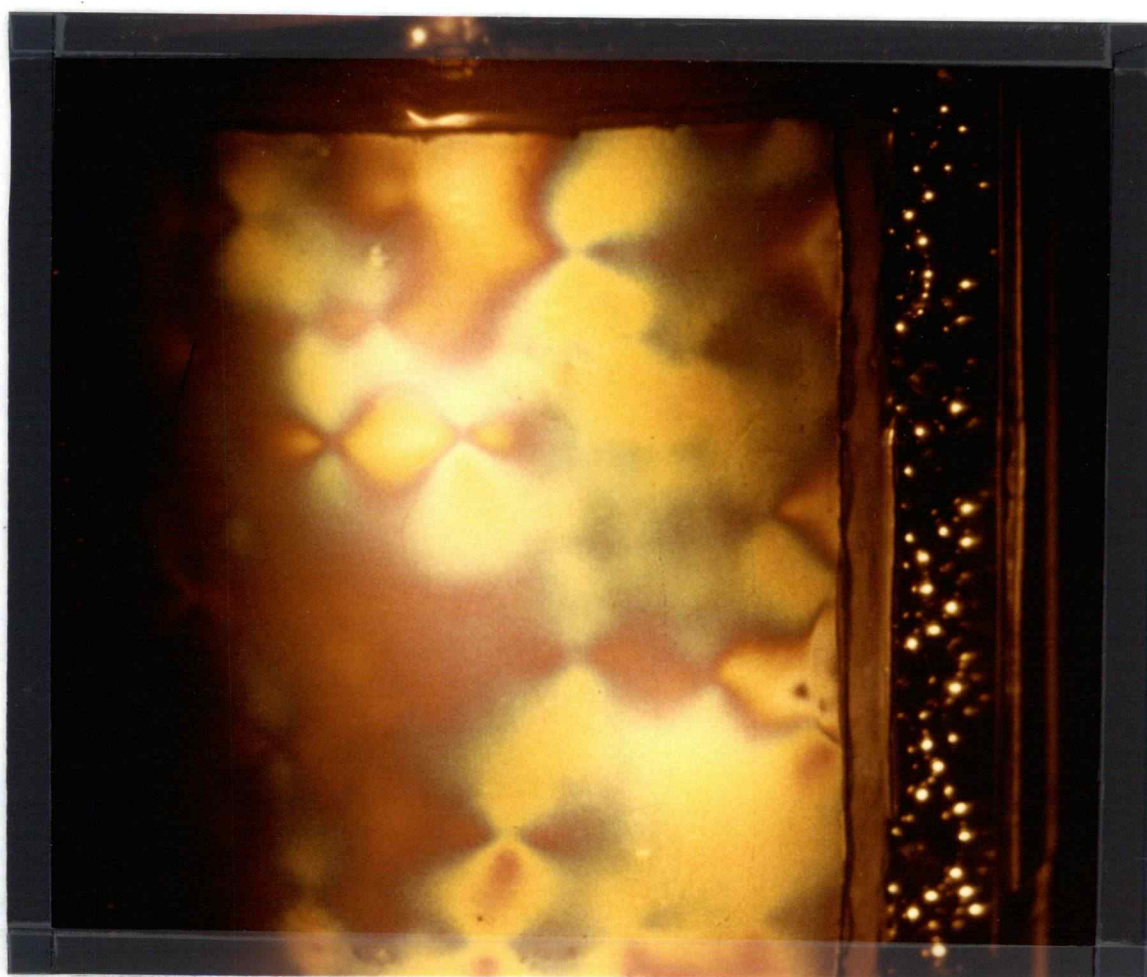


Figure 5.5. Coarse plus medium simulation.

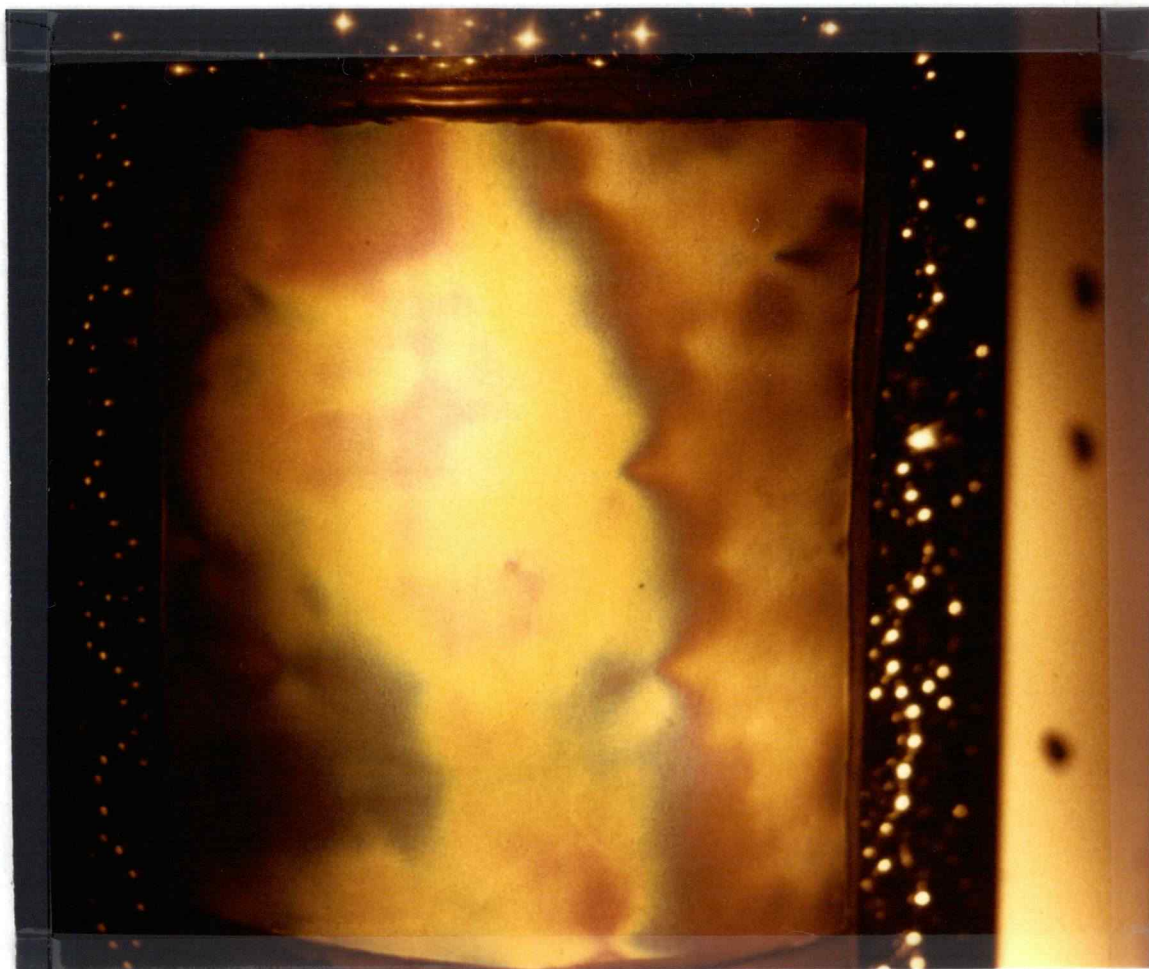


Figure 5.6. Coarse plus medium simulation.

due to the non-infiltrating nature of the components. Thus, regions of uniformity may appear, but diversity is also apparent. Regions exist where the medium fraction is the only constituent contacting the cladding. Other areas show coarse fraction contact density on the order of the previous two cases. As an approximation, the coarse fraction contact point density was near one contact per two square inches, half that for the two prior cases.

From figures 5.5 and 5.6, it is obvious that great disparity in stress distribution exists from one region to another. This typifies this bed type. Many large gradients exist due to point contacts (coarse) but also, unique to this bed type, line defects are apparent. From figure 5.6, it is evident that the sphere pac matrix has locked up in one large region, thus transmitting the majority of the load preferentially. This leaves regions to go into circumferential compression. This result is confirmed by strain gage data.

From figure 5.5, approximately 60% of the coarse contacts are transmitting load noticeably. In stark contrast, from figure 5.6, it is extremely difficult to discern more than even seven coarse contacts corresponding to approximately a 20% figure. These demonstrate the very erratic patterns found in this bed type.

-- Coarse, medium, and fine (Exxon, figures 5.7 and 5.8)

As in the above case, irregular packing is seen. This is primarily due to the two larger fractions' inability to infiltrate one another, thus their position is relatively stable given the initial pin loading configuration. The effect of this relative inhomogeneity is not nearly so apparent as the previous case. The presence of the fine infiltrating fraction has marked influence on the mechanical performance of the bed.

The approximate coarse contact point density at the cladding inner surface is around one per two square inches, as in the previous case. Under load, however, the apparent transmitting fraction is a consistent 60-70% as opposed to a sporadic 20-60% in the coarse plus medium simulation.

The presence of the fine fraction greatly reduced the shear gradients to an average of $N = 0.3$. This gives a very narrow range of shear values over the entire surface. Further effect of the fine fraction was to smear the coarse contact impact. That is the contacts were relatively indistinct from a shear stress viewpoint.

From figure 5.7, it is noticed that the fine fraction was not present near and above the top of the photoelastic coating. This served to demonstrate the drastic effect of the fine fraction. A very distinct transition which translates into stress or strain gradients exists between the regions of presence and absence of the fine fraction.

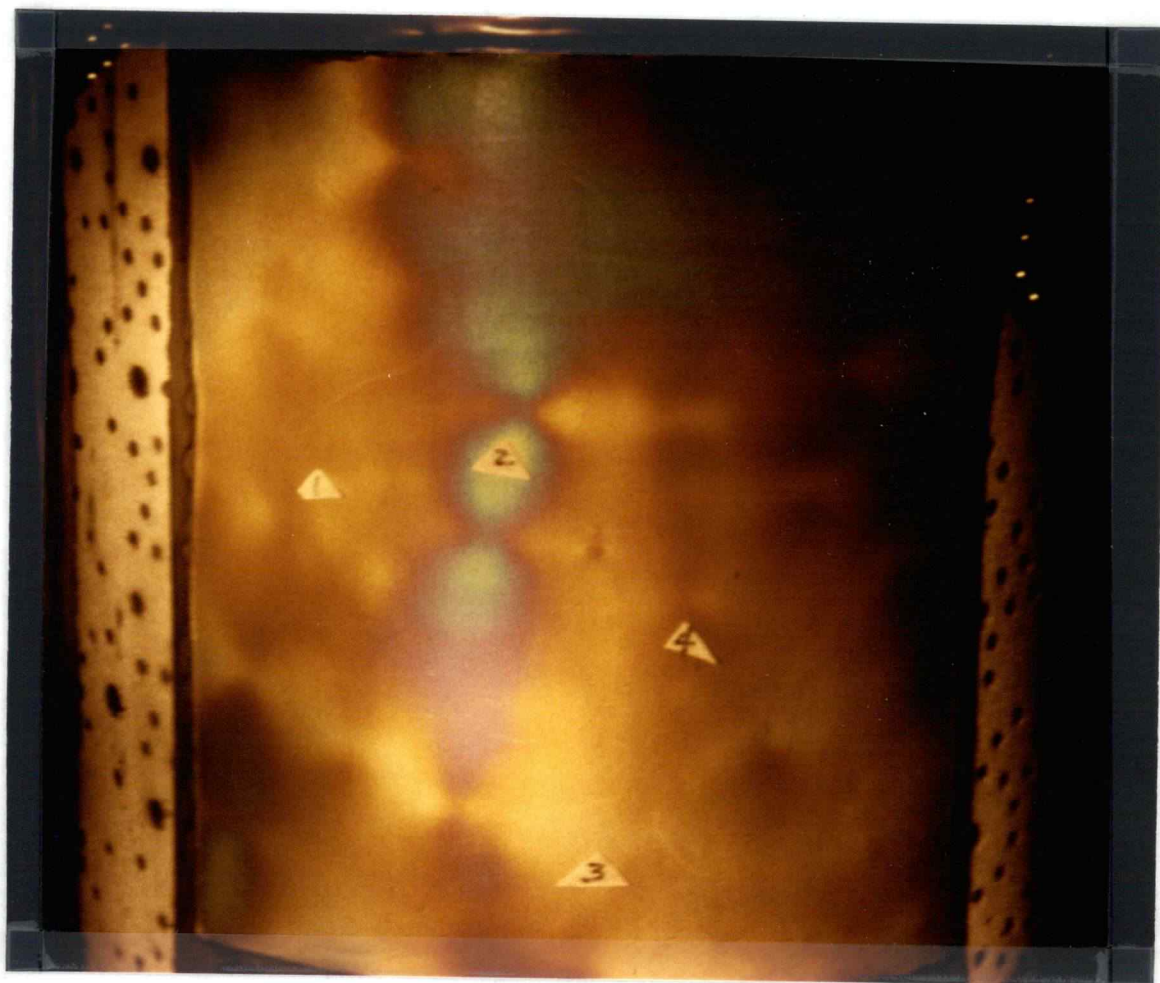


Figure 5.7. Coarse plus medium plus fine
fraction simulation (LWR)



Figure 5.8. Coarse plus medium plus fine
fraction simulation (LWR)

The region above shows markedly higher shear stress than below, on the order of $N = 0.5$ fringe.

-- General results

Common to all cases was the stress distribution (locally) from the coarse fraction contacts. The shape appears somewhat as an hourglass with the vertical axis coinciding with the vertical axis of the test apparatus. These are very distinct in every case. It was the most distinct in the coarse-fraction-only simulations as may be seen from figures 5.1 and 5.2.

It may be inferred from these results that the remaining size fractions may also incur this type of distribution but it is likely to be washed out, through the thickness of the cladding. The sphere diameter to cladding thickness is very small also giving rise to a great deal of interference, again serving to wash out the resultant distribution at the cladding surface.

5.3 Conclusions

The presence of an infiltrating fraction greatly influences the fuel-cladding mechanical interaction of a sphere pac bed with a cladding wall.

Beginning with the non-infiltrating bed types (coarse, and coarse plus medium), it was shown that the resulting stress distribution was very non-uniform (see figures 5.1, 2, 5, and 6). Thus the load being transmitted through the

packed bed to the cladding may also be assumed to be very non-uniform. This may lead to very severe stress situations at the cladding. These two bed types consist of the non-infiltrating components of the LMFBR and LWR simulations, respectively.

For the LMFBR and LWR simulations, the differences are apparent. In both cases, the presence of the fine fraction served to greatly mitigate the severe loading situations demonstrated by figures 5.1, 2, 5, and 6. The effect of the fine fraction was to provide a more intimate load contact throughout the sphere matrix. At the cladding this translates into more shear directions thus giving the greater uniformity seen in figures 5.3, 4, 7, and 8.

Previous to this section, discussion of the contacts at the cladding have been referred to as "point" contacts. The actual case is in fact a contact area. This notion helps to pin down the stress distributions resulting from a sphere impinging on the cladding.

As a basis for discussion, consider a single sphere impinging on a flat wall, axi-symmetrically (fig. 5.9). The maximum shear stress occurs at the periphery of the contact area (ref. 26) which produces a circle of shear maxima. The center of this circle is

$$\tau = 0$$

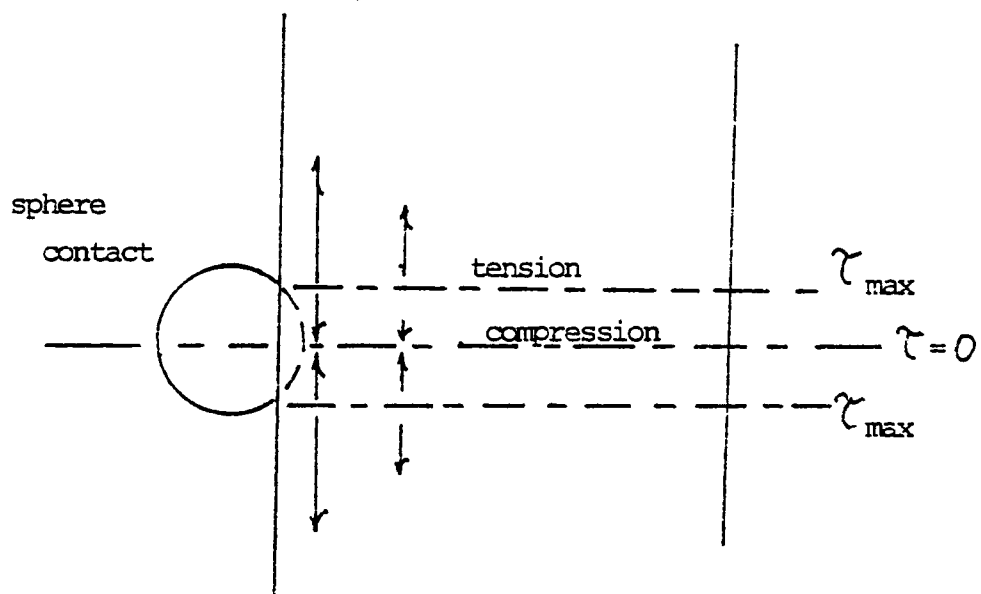


Figure 5.9. Flat wall approximation.

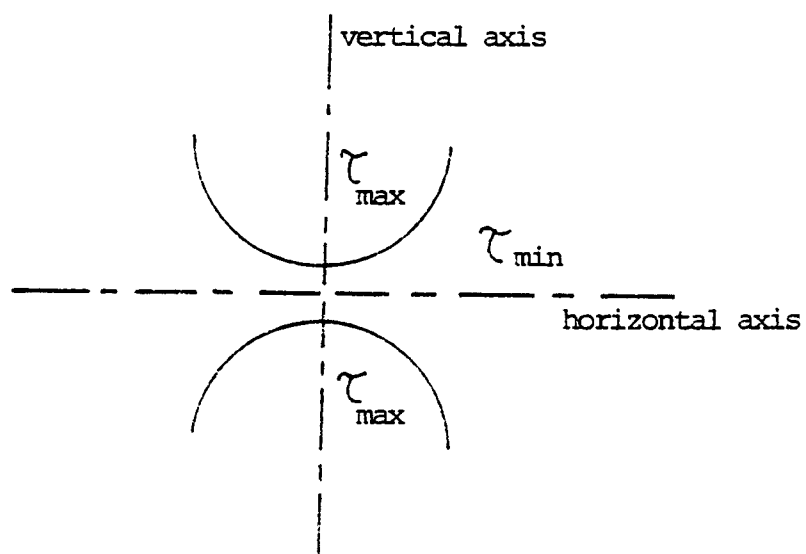


Figure 5.10. Shear distribution on a cylinder wall.

Radiating out from this circle, the shear decreases monotonically.

Adding curvature to this wall, again consider a sphere impinging upon it. As seen from the discussion of results, the stress distribution appears as an "hourglass" type shape (see photoelastic figures 5.1 to 5.8, and 5.10).

Some conjecture is now necessary for the explanation of the comparison. From figure 5.10, the maximum shear stress occurs away from the center of the contact area. This contact area is a partial ellipsoid surface. The maxima occur along the vertical axis (of the test apparatus). The separation of maxima may be thought of as analogous to the flat wall case as follows (fig. 5.11).

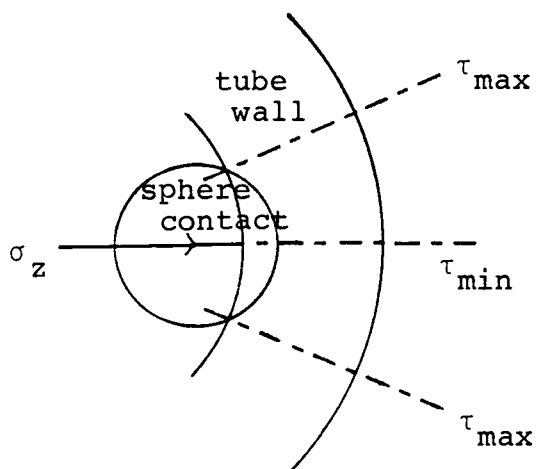


figure 5.11

The curvature of the cylinder propagate the maximum shear stress away from the periphery of the contact area (in radial direction). In the flat wall case, an infinite number of axes of symmetry are present. In the cylindrical case, only two axes are possible; namely, vertically and horizontally. It is thought here that as the radius of curvature goes to infinity the two cases become identical.

Now complicate the situation by impinging a sphere pack matrix upon the cladding. As seen from any of the photoelastic result, two or more "close" contacts may skew the hourglass (or conic section) distribution away from the vertical axis. This becomes more apparent in the infiltrating bed types where far greater surface densities of coarse contacts are transmitting significant loads. Here, not only do other similar fraction contacts skew the distribution, but the fine fraction contribution provides many more avenues for load transmission which further flatten, skew, etc. the resulting distribution.

As for a comparison between the two size fraction (coarse plus fine) bed and the three size fraction (coarse plus medium plus fine) bed, the difference is subtle. Both cases demonstrate a nicely uniform stress distribution at the cladding. The difference is, however, that the overall range of shear is flatter in the Exxon simulation. Also,

the contacts are less discernible in most regions of this simulation. However, regional differences are possible in the LWR case due simply to the packing nature, i.e. the LMFBR case provides for great uniformity throughout, nonuniformity arising basically only with the slight packing imperfections arising in the coarse matrix; the Exxon case non-infiltrating matrix has more inherent nonuniformity, but is mitigated by the quite small fine fraction, thus regions of medium and fine only at the cladding provide a very smooth profile.

BIBLIOGRAPHY

1. Fuel Performance Improvement Program, Quarterly/Annual Progress Report, (C00-4066-13, UC-78), Oct. 1978 - Sept. 1979, Consumers Power Co. Exxon Nuclear Co., Battelle (PNL).
2. JVG Apparatus, Oregon State University, 1979.
3. J. VanGulik, B.A. Waggener, private communication.
4. R. Henke, private communication.
5. L. Thompson, private communication.
6. Enerpac Catalog, E-311, F.S.C.M. No. 26952.
7. Strain gage technology seminar, San Jose, California, Measurements Group, Raleigh, N.C., Oct. 1980.
8. Model 1300 Gage Installation Tester Manual, Vishay/Ellis, Raleigh, N.C..
9. V/E 10 Portable Strain Indicator Manual, Vishay/Ellis, Raleigh, N.C.
10. V/E 11 Switch and Balance Unit Manual, Vishay/Ellis, Raleigh, N.C.
11. Model 030 Reflection Polariscopes Technical Manual, Measurements Group, Raleigh, N.C.
12. Photoelastic Coatings. F. Zandman, S. Redner, and J.W. Dally. Society for Experimental Stress Analysis Monograph No. 3, Iowa State Press, Ames, Iowa, 1980.
13. Measurements Group, Photoelastic Division Technical Data Bulletin T-401-A, "How to Select Photoelastic Coatings," 1980.
14. Measurements Group, Photoelastic Division, Photoelastic technology seminar, Raleigh, N.C., June, 1980.
15. Cadillac Plastics, private communication.
16. Measurements Group, Photoelastic Division, Bulletin IB-221, "Instructions for Molding and Contouring Photoelastic Sheet," 1980.

17. Mechanics of Materials. Higdon, Ohlsen, Stiles, Reese, and Riley. John Wiley & Sons, Inc., 1976.
18. Stress, Strain, and Strength. Robert C. Juvinall, McGraw-Hill Book Co., 1967.
19. Fundamentals of Rock Mechanics. Jaeger, Cook, Methuen and Co., 1969.
20. J. Engr. Mech. Div., ASCE, 1978.
21. T. Kennedy, private communication.
22. OSU-EIR-56, "A Preliminary Model for the Mechanical Behavior of Sphere Pac Pin," T.L. George, T. Kennedy, and K.L. Peddicord, Aug. 1981.
23. Formulas for Stress and Strain. R.J. Roark, McGraw-Hill Book Co., 1965.

A P P E N D I C E S

Appendix A: Optics

While the use of photoelastic coating technology does not require an intricate knowledge of the physics of the situation, an understanding of the basic principles involved provides motivation to the careful application of the methods. This is the purpose of this appendix. The majority of the information contained here is condensed from lecture notes prepared by Dr. Tim Kennedy of the Mechanical Engineering Department at Oregon State University.

A.1 Behavior of Light

Ordinary light is composed of transverse vibrations in all directions, the vectors of which are normal to the direction of vibration. A sinusoidal component of light propagating, in say the positive z-direction, may be expressed as

$$A - a \sin 2 \frac{\pi}{\lambda} (z-ct) \quad (A.1)$$

where c = velocity of light

λ = wavelength of light

$T = \lambda/c =$ period

= time required for passage of two successive peaks.

Conditioning of light may be achieved in several ways. It may be plane polarized by an optical element which

absorbs the components of the light vector not vibrating in the direction of the axis of the polarizer. For a polarizer fixed at some point along the z-axis (say $z=0$), the amplitude may be expressed as

$$A = a \sin 2 \frac{\pi}{\lambda} ct = a \sin 2 \pi ft = a \sin \omega t \quad (\text{A.2})$$

The absorbed and transmitted components of the light vector are

$$A_a = a \sin \omega t \sin \delta \quad (\text{A.3})$$

$$A_t = a \sin \omega t \cos \delta \quad (\text{A.4})$$

where δ = clockwise angle away from axis of polarization of the light vector.

Further conditioning of the light vector may be achieved by a wave plate. This is a plate constructed of material which has the ability to resolve the light vector into two orthogonal components at a different velocity. This material type is known as doubly refracting or birefringent.

The doubly refracting plate has two principal axes, 1 and 2. The transmission of light along axis 1 proceeds at velocity c_1 and along axis 2 at velocity c_2 . Since $c_1 > c_2$, axis 1 is called the fast axis and 2 the slow axis.

For the polarized light vector A_t inclined at angle β with respect to the axis of polarization passing through the plate,

$$\begin{aligned} A_{t_1} &= A_t \cos \beta = a \cos \delta \sin \omega t \cos \beta \\ &= k \sin \omega t \cos \beta \end{aligned} \quad (\text{A.5})$$

$$\begin{aligned} A_{t_2} &= A_t \sin \beta = a \cos \delta \sin \omega t \sin \beta \\ &= k \sin \omega t \sin \beta \end{aligned} \quad (\text{A.6})$$

where $k = a \cos \delta$

There will be a phase shift between components A_{t_1} and A_{t_2} based on their differing velocities of propagation through the plate. Expressing the two components as

$$A_{t_1} = k \cos \beta \sin 2 \frac{\pi}{\lambda} (z-ct) \quad \text{fast} \quad (\text{A.7})$$

$$A_{t_2} = k \sin \beta \sin 2 \frac{\pi}{\lambda} (z-ct) \quad \text{slow} \quad (\text{A.8})$$

For a plate of thickness, h , the phase shift may be expressed as

$$\frac{\Delta \lambda}{2\pi} \quad (\text{A.9})$$

The angular retardation of each component is

$$\Delta_1 = \frac{2\pi h}{\lambda} (n_1 - n) \quad (\text{A.10})$$

$$\Delta_2 = \frac{2\pi h}{\lambda} (n_2 - n) \quad (\text{A.11})$$

where $n =$ index of refraction of air, then

$$\Delta = \Delta_1 - \Delta_2 = \frac{2\pi h}{\lambda} (n_1 - n_2) \quad (\text{A.12})$$

Upon emergence from the plate, the two components of light are

$$A_{t_1}^1 = k \cos \beta \sin(\omega t + \Delta) \quad (\text{A.13})$$

$$A_{t_2}^1 = k \sin \beta \sin(\omega t) \quad (\text{A.14})$$

The amplitude of the light vector formed by these two components is

$$A_t^1 = (A_{t_1}^1{}^2 + A_{t_2}^1{}^2)^{\frac{1}{2}} \quad (\text{A.15})$$

The angle that the emerging light vector makes with axis 1 is

$$\tan \gamma = \frac{A_{t_2}^1}{A_{t_1}^1} = \frac{\sin \omega t}{\sin(\omega t + \Delta)} = \tan \beta \quad (\text{A.16})$$

A.2 Circularly Polarized Light

By selecting the wave plate such that

$$\Delta = \pi/2 \text{ and } \beta = \pi/4 \quad (\text{A.17})$$

and

$$A_t^1 = k/\sqrt{2}, \text{ a constant}$$

$$\tan \gamma = \frac{\sin \omega t \tan \pi/4}{\sin(\omega t + \pi/2)} \quad (\text{A.18})$$

$$= \tan \omega t$$

then

$$\gamma = \omega t \quad (\text{A.19})$$

This result states that the angle of emergence increases with time and the resultant light vector sweeps out a circular helix.

A.3 Stress Optic Law

A sheet of transparent plastic becomes doubly refracting (birefringent) when subject to a 2-dimensional state of stress. The principal axes of stress at any point in the model become the fast and slow axes of the plate (i.e., the index of refraction changes). The polariscope measures these changes in the indices of refraction.

Maxwell found the changes in indices of refraction were linearly proportional to the stresses induced in the model, i.e.,

$$n_1 - n_0 = c_1 \sigma_1 + c_2 \sigma_2 \quad (\text{A.20})$$

$$n_2 - n_0 = c_1 \sigma_2 + c_2 \sigma_1 \quad (\text{A.21})$$

where n_0 = index of refraction in the unstressed state

n_1, n_2 = indices of refraction along the two principal axes associated with

c_1, c_2 = stress optic coefficients

Subtracting the two equations,

$$n_1 - n_2 = (c_1 - c_2) (\sigma_1 - \sigma_2) \quad (\text{A.22})$$

Recall that for a wave plate,

$$n_1 - n_2 = \frac{\lambda \Delta}{2\pi} \quad (\text{A.23})$$

therefore

$$\frac{\lambda \Delta}{2\pi} = (c_1 - c_2) (\sigma_1 - \sigma_2) = C (\sigma_1 - \sigma_2) \quad (\text{A.24})$$

or

$$\Delta = \frac{2\pi}{\lambda} hc (\sigma_1 - \sigma_2) \quad (\text{A.25})$$

This is the classical description of the stress-optic law. The relative angular retardation Δ is linearly proportional to the difference in principal stresses, $\sigma_1 - \sigma_2$. The relative stress-optic coefficient C is a property of the polymeric material used to fabricate the model and is usually treated as a constant. The relative retardation is linearly related to the thickness of the plate and inversely related to the wavelength of light employed with the polariscope.

The stress-optic law is more commonly written today as

$$\sigma_1 - \sigma_2 = N f_\sigma / h \quad (\text{A.26})$$

where $N = \Delta / 2\pi = \delta / \lambda$

= the relative retardation in terms of a complete cycle, also called fringe order

$f_\sigma = \lambda / C =$ material fringe order.

It is apparent from this law that the principal stress difference can be determined if the material fringe value of the model or coating can be established by a calibration procedure and if N can be measured at each point by observation in a polariscope. With birefringent coatings, the light traverses the model twice, so the form of the stress-optic law is modified as

$$\sigma_1^c - \sigma_2^c = Nf_\sigma/2h_c = NF_\sigma \quad (\text{A.27})$$

where $F_\sigma = f_\sigma/2h_c$
 N = coating fringe value.

For the determination of difference in principal strains, use of Hookes' law gives

$$\epsilon_1 - \epsilon_2 = \frac{1+\nu}{E} (\sigma_1 - \sigma_2) \quad (\text{A.28})$$

where ν = Poissons ratio
 E = modulus of elasticity.

Substituting the expressions gives

$$\begin{aligned} \epsilon_1 - \epsilon_2 &= \frac{1+\nu}{E} fN/2h_c \\ &= f_\epsilon N/2h = F_\epsilon N \end{aligned} \quad (\text{A.29})$$

where f_ϵ = the material fringe value
 F_ϵ = the coating fringe value

A.4 Effects of a Stressed Model or Coating in a Circular Polariscopes

To show the effects of a stressed model in a circular polariscopes, consider the light emerging from the series combination of a linear polarizer and a quarter-wave plate. The components of the light vector emerging from the first quarter-wave plates were previously shown to be

$$A_1^1 = \sqrt{2}/2 k \cos \omega t \quad (\text{A.30})$$

$$A_2^1 = \sqrt{2}/2 k \sin \omega t \quad (\text{A.31})$$

When these impinge upon the model, the components A_1^1 and A_2^1 are resolved into two new components A_1'' and A_2'' along the σ_1 and σ_2 axes (ref. 12). These new components will propagate through the model with different velocities and emerge out of phase by an amount Δ which is proportional to $\sigma_1 - \sigma_2$.

The light then propagates to the second quarter-wave plate where it is resolved into components A_1''' and A_2''' . When this light passes through the quarter-wave plate, there is a relative phase shift of $\Delta = \pi/2$ and emerges as components A_1^{IV} and A_2^{IV} .

Finally the light enters the analyzer where horizontal components are transmitted and vertical components are absorbed. The resulting transmitted light vector is

$$A = 0.5k \sin \frac{\Delta}{2} (\cos(\alpha + \omega t) - \sin(\alpha + \omega t)) \quad (\text{A.32})$$

The intensity of the light is proportional to the square of the amplitude

$$I = k \sin^2 \frac{\Delta}{2} (\cos(\alpha + \omega t) - \sin(\alpha + \omega t)) \quad (\text{A.33})$$

Extinction occurs ($I=0$) if

$$1) \quad \cos(\alpha + \omega t) - \sin(\alpha + \omega t) = 0 \quad (\text{A.34})$$

This case cannot be recorded by the eye (because it is so large) and can be ignored.

$$2) \quad \sin \frac{\Delta}{2} = 0$$

$$\text{or } N = \frac{\Delta}{2\pi} = n \quad (\text{A.35})$$

Where N is an integer, also called the fringe order.

A.5 White Light

It was shown above that the conditions of extinction are met if

$$\Delta/2 = n\pi, \quad n = 0, 1, 2, \text{ etc.}$$

At all such points the retardation is

$$\delta = hc(\sigma_1 - \sigma_2) = \lambda \Delta/2\pi = N\lambda \quad (\text{A.36})$$

or

$$= 1\lambda, 2\lambda, 3\lambda, \text{ etc.}$$

When a white-light source is used in a polariscope, many different frequencies and wavelengths of light are present simultaneously. At a point eq. (36) cannot be satisfied for all different wavelengths. When $\delta=0$, extinction will occur

for all wavelengths and a black isochromatic fringe will be observed. For $\delta=0$ (e.g., $\delta=5200\text{\AA}$), the extinction will occur only for the green of wavelength $\delta = 5200\text{\AA}$. A mixture of other wavelengths produced by the source will be observed, producing a visual observation of red, the complementary color or wavelength.

Since only points where $\delta=0$ appear black (complete extinction) in white light, an important observation should be made:

- In the circular dark-field polariscope (ref. 11) only points where $N=0$ and $\delta=0$ ($\sigma_1-\sigma_2 = 0$) will produce a black fringe. This property is used to recognize and measure fringe orders when using compensators, as described in Chapter 3.